Magnetomotive Ultrasound Imaging to Estimate Tissue Elastic Properties - Experiments and Simulations

Stina Andåker & Malin Eriksson

2015

Master's Thesis

Faculty of Engineering LTH
Department of Biomedical Engineering
IT/MT Department, Skåne University Hospital

Supervisor: Tomas Jansson
Examiner: Magnus Cinthio

Abstract

Magnetomotive ultrasound imaging is an imaging technique that utilizes regular ultrasound in combination with an applied time varying magnetic field to induce motion of magnetic nanoparticles injected in the region. This motion can be detected and give valuable information about the particle laden region.

Superparamagnetic iron oxide nanoparticles have been approved for over a decade for use with other imaging techniques and are now utilized for magnetomotive ultrasound imaging research as well. In this report, the possibilities for the use of magnetomotve ultrasound imaging as a pre- and intraoperative method for detecting metastases in the sentinel lymph node was investigated.

In this report magnetomotive ultrasound measurements were performed on tissue mimicking phantoms with elastic properties simulating healthy and cancerous tissue. A model of the setup was created in a multi physics software tool and used to confirm and explain the observed behavior.

The results in this report indicate that a difference in tissue response exists and can be detected. For two different setups with elastic properties of 2.5 kPa and 2.8 kPa we see a relative change in detected displacement of about 30 %. However, for this approach to be utilized clinically, more studies are needed.

Sammanfattning

Magnetomotoriskt ultraljud är en ny bildgivande teknik som kombinerar vanligt ultraljud med ett pålagt tidsvarierande magnetfält för att åstadkomma en detekterbar rörelse i vävnad. Genom att injicera magnetiska nanopartiklar i området man vill undersöka kan på så sätt viktig information tillgodogöras.

Superparamagnetiska järnoxidpartiklar har i drygt ett årtionde varit ett godkänt kontrastmedel för andra bildgivande system och har visat sig kunna utnyttjas även för magnetomotoriskt ultraljud. I denna rapport undersöktes möjligheterna för denna nya bildgivande teknik att, i samband med superparamagnetiska järnoxidpartiklar, användas för både förundersökningar och under operationer för att identifiera den s.k. portvaktskörteln.

Magnetomotoriska ultraljudsundersökningar genomfördes i denna rapport på egentillverkade vävnadsfantomer. Fantomerna preparerades för att få liknande egenskaper som de i litteratur funna elasticitetsvärden för frisk respektive tumörvävnad. Ett mjukvaruprogram användes för att numeriskt modellera och analysera utgången av experimenten och jämföra dessa med de uppmätta värdena.

Resultaten i rapporten visar att man med magnetomotoriskt ultraljud, i kombination med nanopartiklar som kontrastmedel, kan detektera en vävnadsrespons som beror på elasticitetsparametrar hos vävnaden. För två olika uppställningar med elasticitetsvärden på 2.5 kPa respektive 2.8 kPa kunde en relativ rörelseskillnad på 30 % detekteras. För att denna metoden ska vara av värde i kliniska sammanhang behöver den evalueras ytterligare.

Acknowledgements

We would like to take the opportunity to thank two of our supervisors Tomas Jansson and Maria Evertsson for providing us with the information needed to perform this thesis. A special thanks to our third supervisor Roger Andersson for his patience and willingness to always set aside time to aid and guide us in our project, always with a smile on his face. Without the three of you this thesis would never have been able to be completed.

A big thank you to Axel Tojo as well, for all his support regarding the use of the 3D printer, and a shoutout to Olaf Diegel and Mikael Evander for assisting us when Axel was not available.

Thank you Ingrid Svensson, for taking the time to point us in the right direction and Désirée Jarebrant for always providing us and everyone else at the institution with useful information.

A big thank you to the other students performing their thesis' in the same room for contributing to the enjoyment of working with this project; Axel Ekman, Sandra Sjöstrand and Alice Widerström.

Last but not least, a thank you to the whole Department of Biomedical Engineering for having us as master students, it has been a pleasure and a great experience.

Contents

1 Introduction

This master's thesis was performed as the final examination step in the Master of Science in Engineering program at the Department of Biomedical Engineering, Faculty of Engineering, Lund University, Sweden, and was carried out during the spring of 2015.

1.1 Our Hypothesis

We hypothesize that the elastic properties of cancerous tissue will differ from the properties of healthy tissue in such a way that it is detectable by magnetomotive ultrasound if it is used together with a magnetic nanoparticle contrast agent. The difference in the magnetomotive response in the tissue will, after proper offline analysis of the ultrasound data, suffice as an indication of whether or not a region in the body contains cancer metastases.

1.2 Aim

The goal with this thesis is to determine if the variations in elastic properties in healthy, compared to cancerous tissue, can be utilized to detect cancer metastases in the lymphatic glands with magnetomotive ultrasound imaging.

Satisfying results could indicate the possibilities for magnetomotive ultrasound with nanoparticle contrast agents to be used as a new standardized pre- and intra-operative imaging method.

The conclusions of this thesis will hopefully be of use in the early investigations of future clinical applications for magnetomotive ultrasound imaging.

1.3 Course of Action

This thesis can be split into two main segments, one practical and one theoretical.

The practical part of this project revolved around the performance of magneto-motive ultrasound measurements on a tissue mimicking phantom. The phantom mold was designed using a CAD software and printed by a 3D printer. A tissue-like substance was prepared in a chemistry lab and inserted into the printed mold. Elasticity measurements to evaluate the Young's modulus for the tissue mimicking material was also conducted.

The theoretical part consisted of simulations and evaluations in a software tool based on the finite element method. The simulations were used to illustrate and confirm the assumptions made beforehand, and to compare the simulated results to the practical measurements.

2   Background

In this chapter, the concept of magnetomotive ultrasound and its relevance to this thesis is explained. The clinical importance of the sentinel lymph node concept and its relevance to breast cancer treatment will be highlighted, along with an overview of current methods for detecting and imaging the sentinel node. The theory of how nanoparticles in tissue are affected by applied magnetic fields and their response will be handled. The MATLAB algorithm later used for analysis of the collected ultrasound data from the practical experiments, will be given a brief explanation. A section about basic ultrasound imaging will end this theory chapter.

2.1   Magnetomotive Ultrasound

Ultrasound (US) imaging is, due to its many advantages over other imaging modalities, the medical imaging method most used for clinical evaluations (Mehrmohammadi et al., 2013). It offers real-time images, is non-ionizing, portable, easy to use and cost efficient (Junghwan et al., 2006). However, the limitation in contrast between normal and pathological tissue has limited the use for US imaging for biological events at molecular levels, giving more attention to other modalities, with well established contrast agents, such as magnetic resonance imaging (MRI), computed tomography (CT) and radionuclide imaging (RI) (Qu et al., 2011). High cost, ionizing radiation and the limited reconstructive nature of MRI, CT and RI are however some of the factors indicating that US imaging combined with a sufficient contrast agent is the best candidate for molecular level assessments (Mehrmohammadi et al., 2013).

Gaseous microbubbles are the most commonly used contrast agent for US imaging since they produce a strong backscattered signal due to their large impedance difference to surrounding tissue. The use for microbubbles in molecular imaging is however not optimal because of their relatively large size, thus not able to penetrate the endothelium in the microvasculature. Other properties such as instability and short blood half-life makes the need for a more suited contrast agent apparent (Junghwan et al., 2006).

Magnetomotive ultrasound (MMUS) imaging is a technique that utilizes metal-based nanoparticles as contrast agents. It has shown promising results in applications for improving the diagnosis for spread in e.g. breast cancer and malignant melanoma, and is suggested for intra-operative use. The particles used are superparamagnetic iron oxide nanoparticles (SPIO-NP) and have been approved for use in MRI for over a decade. Due to their small size they can be used for mapping biological events on a cellular and molecular level, thus enabling earlier detection of pathological behavior since changes at these levels occur far earlier than anatomical changes. Earlier detection will furthermore lead to provision of useful information about the behavior of a disease at an early stage (Evertsson et al., 2014).

The principle behind MMUS is to utilize the magnetic properties of the contrast agent by applying a time-varying magnetic field to the volume containing the injected SPIO-NP. The magnetic force acting on the SPIO-NP's, see equation (4),

will cause the particles and their immediate surroundings to move. This induced movement can then be detected with US, and proper processing of the US data, further described in section 2.5, gives valuable information on the SPIO-NP-laden regions(Evertsson et al., 2013).

2.2   The Sentinel Node Concept

The lymphatic system is a very dynamic and reactive system with roughly three liters of lymph fluid circulating in the body each day. The lymph vessels transporting the lymph are larger than the blood capillaries surrounding them, and their fluid is directed in only one way, ensured by valves. When substances of particulate sizes are delivered to the interstitial fluid they transverse the lymphatic capillary endothelium and are removed, *i.e.* drained towards the first lymph draining nodes. These draining nodes are accumulated in so called basins which exists in various parts of the body (Keshtgar et al., 1999).

It has been repeatedly shown that most of the breast lymph drains to nodes in the axillary area, a fact that is of huge importance to the field of breast cancer treatment. The sentinel lymph node (SLN) is defined as the lymph node(s) first draining the primary tumor. This implies that if there are lymph-borne metastatic cells, these are most likely to be found in the SLN. (Buscombe et al., 2007) In fact, studies have shown there to be a less than 0.1 percent risk of non-sentinel node involvement of metastasis if the SLN is free of tumor, *i.e.* "node negative". The concept of the SLN is based on the knowledge that lymphatic metastases occurs not randomly but in a predictable orderly manner, and therefore the status of the SLN is an indicator of the status of the rest of the nodal basin (Somasundaram et al., 2007).

2.3   Current Methods for Sentinel Lymph Node Imaging

With roughly 8000 diagnoses a year, breast cancer is the most common form of cancer for women in Sweden. The number of people suffering from the disease is however lower since some patients get cancer in both breasts (Dahllöv, 2015a). When treating patients, the goal is to obtain not only information about the primary tumor, but also to accurately predict the risk of distant metastases to be able to give the most efficient treatment (Somasundaram et al., 2007). Considering this, the status of the SLN in breast cancer treatment has become one of the foremost prognostic factors (Gherghe et al., 2015).

The most common way to fight the cancer is to use a combination of different treatment types such as surgery, radiation therapy and chemotherapy. Surgery however is something that almost everyone diagnosed with breast cancer undergoes. Most surgeries consist of not only removal of the breast tissue, but also removal of lymph nodes in the axilla (arm pit) (Dahllöv, 2015b).

Axillary lymph node dissection (ALND) is a procedure in which the lymph nodes in the axillary area is surgically removed. However, with the growing possibility of detecting cancer at an earlier stage, the risk of lymphatic metastases at diagnosis

has decreased, making ALND an unnecessary procedure. There are also quite a few side effects with removal of axillary lymph nodes, such as post-operative pain, paraesthesia, shoulder stiffness and the most severe of them all; lymphedema. Thus, a new form of axillary staging has arisen called sentinel lymph node biopsy (SLNB). SLNB is a minimally invasive surgical technique that has far less morbidity compared to ALND and has become the new gold standard method for staging the axilla in breast cancer patients. The procedure consists of finding the SLN and then performing a histology to determine if it is positive or negative of metastases. Since patients with a negative SLN can avoid the possible postoperative complications of an extensive ALND, a lot of effort has gone into optimizing the search for the SLN (Somasundaram et al., 2007) (Gherghe et al., 2015).

There is an obvious advantage of identifying positive SLN's pre-operatively, as a SLNB then is redundant. If a patient has enlarged lymph nodes, suspicious sizes being approximately > 5 mm, regular US can be used to detect the SLN beforehand. A histology is performed on the node and if there are signs of metastases the surgeon will proceed with an ALND during the main surgery (mastectomy). (Somasundaram et al., 2007) (Dahllöv, 2015b) This is where the use of MMUS could come in hand, seeing as detection of a positive SLN at a molecular level at this stage could prevent unnecessary SLNB's and/or ALND's.

However, as of today lymphoscintigraphy (LS) is the current gold standard for finding the SLN, the most effective approach consisting of combining two modalities and will be described below. The term LS is not to be confused with the former meaning of the word, *i.e.* when it was used to describe the staging of all lymph nodes in a particular lymph basin. (Keshtgar et al., 1999) In this thesis the word is rather used to illustrate the localization of the SLN.

LS consists of pre-operative SLN imaging using a gamma camera and intra-operative imaging using a combination of a gamma probe and injected blue dye. By injecting radiocolloids pre-operatively, the surgeon gets information from the pictures taken with the gamma camera on the location of the SLN(s). The first lymph node(s) to be detected in the images is considered to be the SLN. Intra-operatively, the surgeon is guided not only by the gamma probe, but also the blue dye injected to the lymphatic tracts draining the tumor. (Somasundaram et al., 2007) (Buscombe et al., 2007) LS is considered in patients who for certain will undergo mastectomy and have axillary lymph nodes which are not palpable (Buscombe et al., 2007).

2.4 Magnetic Fields

An electromagnet, consisting in this case of a solenoid wrapped around an iron core with a pointed tip, can create a magnetic field, **B**, which has the properties of equation (1) if the current, I, is sent through the coil. (Griffiths, 2008) An advantage of using an electromagnet is that the strength of the field, controlled by the size of the current and the number of turns, N, can be controlled and adjusted as desired. Having a pointed tip is also of use, as the magnetic field becomes more concentrated and can thus be more precisely aimed in the desired direction.

$$\mathbf{B} = \frac{\mu_0 n I \hat{\mathbf{z}}}{l} \tag{1}$$

Here, μ_0 is the permeability of free space, and l is the length of one loop in the solenoid. If the current flowing through the solenoid is sinusoidal, the induced magnetic field directed along the z-axis will be given by:

$$\mathbf{B}(z,t) = sin(2\pi f_0 t)\mathbf{B}_z(z)\hat{z} \tag{2}$$

Here, f_0 is the frequency of the applied sinusoidal signal. An object placed at the tip of an electromagnet with the proerties given above will thus be affected by the mgnetic field given by equation (2) (Griffiths, 2008).

2.4.1 The Magnetic Force Acting on Magnetic Nanoparticles in Tissue

To evaluate how a magnetic field, as described above, will influence magnetic nanoparticles in tissue, the characteristics and magnetic properties of the nanoparticles need to be considered as well. The magnetic susceptibility, χ_{np}, is a dimensionless quantity and indicates a material's (in this case the nanoparticles') response to an applied magnetic field. The permeability, μ_0, and the volume of nanoparticles will also affect the force. If V_{tot} is the total volume of nanoparticles and n_{frac} is the volume fraction, i.e. the ratio of magnetic core volume to the nanoparticle's total volume, the following relation holds:

$$V_{np} = V_{tot} \cdot n_{frac} \tag{3}$$

Here, V_{np} denotes the total effect that the volume of nanoparticles will have on the magnetic force.

Thus, the final expression for the magnetic force, from an electromagnet producing a field with frequency f_0, acting on magnetic nanoparticles in the z-direction will be given by:

$$\mathbf{F}_{mag}(z) = \frac{\chi_{np}V_{np}}{2\mu_0}(1 - cos(4\pi f_0 t))\mathbf{B}_z(z)\frac{d\mathbf{B}_z(z)}{dz} \tag{4}$$

As can be seen, the force will depend not only on the strength of the magnetic field but also on its gradient. A larger magnetic force can be produced if the susceptibility is higher, as well as if the magnetic core is larger. Another insight that is gained by studying the magnetic force is that the magnet's excitation frequency is half of

the frequency that the magnetic particles will oscillate with. This fact is utilized to measure the particle's magnetomotive response in tissue (Junghwan et al., 2006).

2.4.2   The Total Force Acting on Nanoparticles in Tissue

With the magnetic force given above, see equation (4), the total force affecting magnetic nanoparticles in tissue will be given by the following equation:

$$\sum \mathbf{F}_{tot}(z) = \frac{\chi_{np} V_{np}}{2\mu_0}(1 - cos(4\pi f_0 t))\mathbf{B}_z(z)\frac{d\mathbf{B}_z(z)}{dz} - kz(t) - r\frac{dz}{dt} \qquad (5)$$

Here, the terms $-kz(t)$ and $-r\frac{dz}{dt}$ are the elastic restoring force and the viscous drag force acting on the particles (Junghwan et al., 2006).

2.4.3   The Threshold Criteria

As can be seen in equation (5) magnetic nanoparticles in tissue will be affected not only by a magnetic force, but also by forces originating in the tissues elastic properties, when exposed to an applied magnetic field. Thus, it becomes sensible to consider a threshold, *i.e.* a critical state at which the force from the magnetic field will balance the elastic forces from within the tissue causing there to be no magnetomotive response.

Such a threshold has been experienced in previous studies such as (Evertsson et al., 2013) but its origin is debated. Oldenburg *et al* suggest that the phenomenon is due to tissue being mainly diamagnetic as oppose to the paramagnetic nanoparticles (Oldenburg et al., 2008). A diamagnetic material responds to an applied magnetic field by inducing an internal opposing field and would therefore be repelled by a magnet. Materials that express paramagnetic behavior would on the contrary be appealed by the same field (Schenck, 2005).

Thus, assuming a high enough magnetic force acting on the particles, the net response would appear paramagnetic, and vice versa diamagnetic if the threshold is not met (Jansson et al., 2014). This reasoning could explain the observed threshold effect, however results by Jansson *et al* indicate otherwise. Their studies show a lack of diamagnetic response in SPIO-NP-free phantoms, suggesting that the threshold effect could more likely be related to the mechanical coupling between the SPIO-NP-laden regions and the surrounding tissue (Jansson et al., 2014).

2.5   MATLAB Analysis of the Collected MMUS Data

To further evaluate the ultrasound measurements performed on the phantom an algorithm developed by Evertsson *et al.* was used. It is based on quadrature detection and phase gating at the same frequency with which the NP's are moving, which allows movements and clutter occurring at any other frequencies to be filtered out. The algorithm, after processing the US data, produces a color-coded signal that is

superimposed on the original B-mode image. The displacements of the SPIO-NP-laden regions can then be retrieved from the new image (Evertsson et al., 2013).

2.6   Basic Ultrasound Physics

Ultrasound imaging is a technique that enables us to see through objects that we normally can't, by using ultrasound waves. The waves are sent through the investigated object *e.g.* a human body and are reflected against boundaries inside the object. In a human body this can be tissues and organ boundaries. The reflections become echoes that will travel in all directions, and the ones that travel straight back will be detected and displayed as a point in an image. When several points are created, they will form a B-mode image *i.e.* a classic ultrasound image.

2.6.1   Image Formation

The basic principle of how a B-mode image is formed with ultrasound waves begins with a transducer, the source of the ultrasound. The transducer is placed in contact with the object to be examined, usually together with a layer of ultrasonic gel to obtain a connection between the object and the transducer. The transducer sends out a pulse of ultrasound through the object which scatters and reflects the wave, generating echoes that travel in all directions. It is only the echoes that travel straight back that are detected by the transducer, which is now in a receiving mode *i.e.* it listens for echoes. All the echoes that have been detected are converted to different points in an image, the points have a corresponding position in the image to what that caused the echo in the object. The brightness of each points in the image depends on the strength or amplitude of the echo, higher amplitude leads to a brighter point. This has given the image its name brightness mode, B-mode.

To convert an echo to a point, the system needs information such as the range from the transducer to the target *i.e.* the distance from the transducer to the object that caused the echo, and the direction of where the target is in relation to the active part of the transducer. The range, d, is measured with a pulse-echo principle which is based on that the time, t, is measured during a pulse is transmitted by the transducer and the echo from the same pulse returns, this is known as the go and return time. During this time the pulse has together with the echo traveled twice the distance. If the speed of sound, c, in the investigated object is known, equation (6) can be used to calculate the range.

$$d = \frac{c \cdot t}{2} \tag{6}$$

The B-mode image in total is formed from a number of so called B-mode lines. A line is the main pulse-echo sequence sent out from the active element of the transducer. The pulse goes through the object and its returning echoes creates a line in the image. When one active part of the transducer has sent out its pulse-echo sequence the active part will move along the array to send out new pulse-echo sequences, which creates a new image line at each position. One completed sweep of the array

is done in around 30 ms which allow real-time B-mode images with negligible delay (Hoskins et al., 2010).

2.6.2 Transducers

The transducer is the device of the ultrasound system that converts the electrical transmission pulses into ultrasonic pulses, it also converts the ultrasonic echo pulses into electrical echo signals. There exists different transducers and the choice depends on what size, shape and depth is wanted for the ultrasound beam. The most common transducers are linear, curvilinear, trapezoidal, sector and radial. The curvilinear and the trapezoidal are often used for obstetric scanning due to their wide field of view near the transducer and an even wider field of view at deeper depths. Whereas the sector transducer is more common for imaging of the heart, due to it has all the B-mode lines close together near the transducer so it can pass through narrow gaps between the ribs and diverge thereafter to give a wide field of view at the depth such as the heart. For examinations within the body, a radial transducer is used since all its lines are radiated out from the center of the field of view, like the light beam of a lighthouse. The transducer for this project was the linear array transducer, it is built up from many small transducer elements that is aligned in a straight line and is perpendicular to the transducer elements. This gives a rectangular field of view that is useful for both superficial and deeper views.

All transducers and their elements are built up by similar components such as a piezoelectric plate that is the main sound generating and detecting component, a matching layer that enhance the sensitivity, a backing layer which reduce unwanted ringing and usually a lens that helps with the focus of the beam. However, depending on the type of the transducer or the application for the transducer it will vary in size, shape, number or arrangement of the transducer elements and its components (Hoskins et al., 2010).

3 Materials and Equipment

This chapter address the materials and equipment that has been used throughout this project. The different materials that are mentioned below were used for the mold and phantom, while the equipment was used in the making of the mold as well as for the practical experiments.

3.1 Superparamagnetic Iron Oxide Nanoparticles

SPIO-NP were developed for the fields of biomedicine and biotechnology. They are today used for instance as a contrast agent in magnetic resonance imaging and are approved for clinical use. The SPIO-NP that was used for this project was developed by GeccoDots AB, Lund, Sweden.

The structure of the SPIO-NP is very basic. It consists of a solid iron oxide core, Fe_3O_4, with a diameter of approximately 11 nm $\pm$ 1 nm and a high magnetic saturation, about 80 emu/g. The core is coated with a layer of polyethylene glycol (PEG), this layer has a total thickness of 3 nm. PEG is a good material to use since it is biocompatible.

It is of high importance that the SPIO-NP has an extreme stability due to the use in in-vivo applications. To ensure high chemical stability and integrity of the nanoparticles, they have gone through several tests in different solutions such as buffers with a pH range from 2 to 12, extreme salt concentrations, high protein concentrations solutions, serum and human serum (Fredriksson et al., 2015).

3.2 Polyvinylalcohol

Polyvinylalcohol are small hydrophilic polymer crystals i.e. the crystals are built up from long chemical compound chains of small repeated units that will easily dissolve in water. The polyvinylalcohol that has been used for this project was a polyvinylalcohol from Sigma-Aldrich, USA. It has a white to off white color and can be up to 99.3-100.0 % hydrolyzed and has an average molecular weight, M_W, of 85,000 to 124,000 (Sigma-Aldrich, 2015).

3.3 The Ultrasound Scanner

The VisualSonics Vevo 2100 system (VisulaSonics Inc., Toronto, ON, Canada) is an ultrasound device that has a high-frequency, high-resolution digital imaging platform with linear array technology. It is mobile and a non-invasive technology with a hard drive of 300 GB to store data on. Together with the VisualSonic 2100 system, the linear array transducer, MS250, (VisualSonics Inc., Toronto, ON, Canada) can be used. The transducer has ha bandwidth of 13 to 24 MHz and a center frequency of 21 MHz (VisualSonics, 2015).

3.4   3D printer

Ultimaker 2 is a 3D printer that supports the materials PLA, ABS and U-PET. This printer was used in the making of the mold for the phantom in this project.

To print in 3D, a model of the object needs to be created in a 3D modeling software *e.g.* Fusion 360. When satisfied with the model it needs to be saved and then opened in a software program *e.g.* Cura that will prepare the model for the 3D printer. Cura assesses and analyzes the model in order to slice the model into several small horizontal layers. It is in this software all printing settings will be made, *i.e.* layer thickness, printing speed etc. It also gives the user a possibility to see the model from the inside, outside or from any angle that is desired so that everything can be assessed.

The model and settings in Cura needs to be saved to an SD card that the Ultimaker 2 can read. The printer will then upload the model and its settings so it can start prepare for the printing. The printer will start by heating the heating bed to a temperature of your choice between 50-100 degrees Celsius and the extrusion nozzle to a temperature which will melt the material, in this case where PLA was used to around 210 degrees Celsius. The extrusion nozzle controls the flow from 30 – 300 mm/s and has a definition up to 0.02 mm. When the printer reach the right temperature in both the heating bed and the nozzle it adjusts its starting position and will then begin to print. The printer reads every 2D layer from Cura and will then print every layer successively, it starts with the bottom layer and builds its way up until the 3D object is created. The maximum building volume the Ultimaker 2 can print is 230x225x205 mm (Ultimaker, 2015).

3.5   Poly Lactic Acid and Polyhydroxyalkanoate

Poly lactic acid, PLA, and polyhydroxyalkanoate, PHA, is a mixture of polyester materials that is used as a 3D printing filament. The company ColorFabb creates a unique mixture of PLA and PHA to make the filament tougher and less brittle. Both the PLA and the PHA is a bio-polyester, this means that it is 100 % biodegradable (ColorFabb, 2015b).

When printing with PLA/PHA it is of important that an exact amount of material comes through the nozzle, ColorFabb guarantees a diameter tolerance of ±0.05 mm of the filament. To get the best result from printing with PLA/PHA filament, it is recommended a printing temperature around 195-220 degrees Celsius, a printing speed around 40-100 mm/s and the heating beds temperature should be around 50-60 degrees Celsius. To keep the printed object in place on the heated glass bed it is a good idea to apply a thin layer of glue (ColorFabb, 2015a).

4 Method

This chapter gives a detailed description of the two methods that have been used. First, the practical experiments are explained, including the making of the phantom molds, the PVA preparation and the elasticity measurements. Second the experimental setup is discussed briefly and the phase-sensitive and frequency-tracked MATLAB code for analyzing the collected MMUS data is described. A discussion of how COMSOL is used to simulate the practical experiments ends this chapter.

4.1 Practical Experiments

The phantom for this project was based on the design from the previous thesis where the phantom had a cuboid shape with three cylinders in the center section, see figure 1(a). This phantom was made from a mixture of PVA solution and graphite. For the cylinders three different concentrations of SPIO-NP were examined and therefore added to the mix. Since this project tests representative elasticities of what would be cancer tissue, it was decided to use only one cylinder in the cuboid, see figure 1(b), that will represent a lymph node. The dimension of the cuboid would be the same as in the previously thesis i.e. 10.0x10.0x25.0 mm and the same for the cylinder 5.0 mm in diameter and 10.0 mm in length.

(a)   (b)
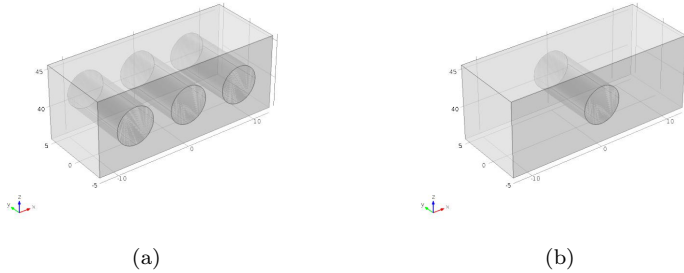
Figure 1: (a) Phantom design from the previous thesis. (b) Phantom design for this project.

Two different setups of the phantom were made, one with cancer tissue mimicking material in the cylinder that is in turn surrounded with healthy tissue mimicking material and the other phantom is made as an inverse i.e. health tissue mimicking material in the cylinder that is in turn surrounded with cancer tissue mimicking material. In both cases SPIO-NP was injected into the cylinder.

4.1.1 Creation of the Phantom Mold

To create the two different versions of the phantom a mold was designed in Fusion 360. The phantom was designed as a hollow cuboid that is missing two sides, see figure 2(a). A cylindrical hole was made in the long side of the cuboid for the purpose to hold a lid in place. This lid will close up the cuboid and at the same time create

a cylindrical hole in the phantom when it is cast and has gone through a couple of freeze and thaw cycles, see figure 2(b). The lid was designed with slightly tilted edges that would match the slightly tilted walls of the cuboid. The design with the tilted walls had showed to be the easiest design to make the mold watertight. To be able to get the different harnesses of the material in the cylinder versus the surrounding there was a need to cast the cylinder in a separate mold. This mold consist of a cylinder together with a base plate to keep the liquid inside, see figure 3. To resemble the two parts of the phantom a second lid was designed, with the purpose to hold the phantom in place, see figure 2(c). The measures of all phantom parts can be seen in table 1.

(a)   (b)   (c)
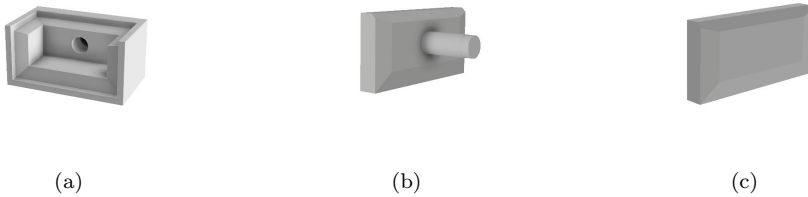
Figure 2: (a) The cuboid part of the phantom mold. (b) The lid with the cylinder that creates the cylindrical hole in the phantom. (c) The lid to hold the phantom in place while it is in the refrigerator and freezer.

(a)   (b)

Figure 3: (a) The cylinder to cast the cylindrical part. (b) The base plate for the cylinder to stop the PVA mixture to leak out.

Phantom mold		
	Fusion 360	**Actual size**
Cuboid (mm)	10.0 x 10.0 x 25.0	10.0 x 10.0 x 25.0
Cylindrical hole (mm)	Depth: 7.0 Diameter: 5.6	Depth: 7.0 Diameter: 5.5
Cylinder Lid (mm)	10.0 x 25.0 Diameter bottom: 5.0 Height bottom: 10.0 Diameter Top: 4.9 Height Top: 1.8	10.0 x 25.0 Diameter bottom: 5.0 Height bottom: 10.0 Diameter Top: 4.9 Height Top: 1.8
Lid (mm)	10.0 x 10.0 x 25.0	10.0 x 10.0 x 25.0
Cylinder (mm)	Inner diameter: 5.5 Height: 34.0	Inner diameter: 5.0 Height: 34.0
Base plate (mm)	15.0 x 15.0 Cylinder diameter: 5.3 Cylinder height: 2.0	15.0 x 15.0 Cylinder diameter: 5.0 Cylinder height: 2.0

Table 1: Measurements of the phantom mold, both actual size and in the design program.

All parts of the phantom were designed in Fusion 360 and after this saved to an STL file so that they could be opened and prepared in Cura for the 3D print, see the settings for Cura in table 2. When all settings were done and it had the correct appearance in Cura, the model was saved to an SD card that could be inserted into the 3D printer. The model was then set to print and after some hours the phantom mold was printed and ready to be used.

Cura settings	
Layer height (mm)	0.1
Shell thickness (mm)	0.8
Bottom and top fill thickness (mm)	0.6
Fill Density (%)	20
Print speed (mm/s)	40

Table 2: Settings for the 3D print.

4.1.2 Preparations of the Tissue Mimicking Material

The goal was to make a phantom that imitates both healthy and cancerous tissue. A 5 % solution for the phantom was wanted when all the components was added. This was prepared from a mixture of 7.5 % PVA solution, graphite, Milli-Q water and for the cylindrical insert, also SPIO-NP solution. The 7.5 % PVA solution was used to ensure the 5 % solution when all components was added together and the graphite was added to act as a scattering medium *i.e.* to give contrast in the ultrasound pictures. To make 50 g of the 7.5 % PVA solution 3.75 g of PVA crystals and 46.25 g of Milli-Q water was poured together in a heat resistant container. The container was sealed and weighed, and then put in an oven (Nüve FN300, Ankara, Turkey) to be heated up to 95 degrees Celsius for about two to three hours. This was done so that the PVA crystals could be dissolved in the Milli-Q water. For every half hour the container was taken out of the oven to be stirred. When all the crystals had been dissolved the container was weighed to see if there had been any weight loss. If so, Milli-Q water was added to compensate. When the 7.5 % PVA solution was ready graphite was added. The amount of graphite to be added was 0.03g/ml, in this case 1.5 g of graphite (Graphite, Merck KGaA, Darmstadt, Germany). The container was then put on a magnetic stirrer until the graphite was evenly distributed.

To obtain a 5 % PVA mixture in the different part of the phantom, they were mixed separately. The cylindrical part had a volume of 0.628 ml and contained a mixture of 7.5 % PVA Solution, graphite, Milli-Q water and SPIO-NP solution. To obtain the wanted concentration, 0.3 mg/ml, of the SPIO-NP solution equation (7) was used to calculate how much of the main batch of the SPIO-NP solution, concentration of 3.5 mg/ml, had to be diluted. This gave that the main batch needed to be diluted 11.7 times. To obtain the volume of the SPIO-NP solution equation (9) was used, which gave a volume of 0.0540 ml. Then to obtain the right amount of Milli-Q water and 7.5 % PVA solution with graphite equations (10) and (11) were used, which lead to a volume of 0.419 ml 7.5 % PVA solution and 0.155 ml Milli-Q water. The SPIO-NP solution, PVA solution and the Milli-Q water was evenly mixed together with a vortex and then poured in to the cylinder.

$$dilute = \frac{c_{main}}{c_{wanted}} \tag{7}$$

$$x = \frac{5\%}{7.5\%} \tag{8}$$

$$V_{NP} = \frac{V_{cylinder}}{dilute} \tag{9}$$

$$V_{PVA} = V_{cylinder} \cdot x \tag{10}$$

$$V_{MilliQ} = V_{cylinder} - (V_{NP} + V_{PVA}) \tag{11}$$

Dilute stands for how much the main concentration of the SPION-NP solution, c_{main}, needs to be diluted to get the wanted concentration, c_{wanted}. x is the ratio between the wanted solution of 5 % and the 7.5 % PVA solution. V_{NP} is the volume of how much SPIO-NP solution that is needed and V_{PVA} is how much volume of the 7.5 % PVA solution with graphite that is needed. V_{MilliQ} is the volume of the Milli-Q water that is needed. $V_{cylinder}$ is the volume contained in the cylinder.

The surrounding phantom contained a mixture of 7.5 % PVA solution, graphite and Milli-Q water. To calculate how much of each solution that was needed, it was done in the same way as for the cylinder but with the cuboids volume instead. Also the amount of SPIO-NP solution that was needed was replaced with the same amount of Milli-Q water. The volume for the cuboid was 2.5 ml which lead to a volume of 1.667 ml for the 7.5 % PVA solution and 0.833 ml of Milli-Q water. The solution was mixed evenly with a magnetic stirrer and then poured into the cuboid with the cylinder lid.

To obtain different elastic properties of the 5 % mixture it underwent a number of freeze and thaw cycles. One freeze and thaw cycle means that the material is put in the freezer for 18 hours and is then put in the refrigerator for six hours to thaw. This process creates chemical bindings in the PVA that will make it stiffer and less elastic. Four different setups of the phantom were made and for each setup a duplicate was created in case something went wrong. Setup 1 consisted of a phantom with a stiffer cylindrical part and a softer surrounding, see table 3. Setup 3 is an inverse model of Setup 1 i.e. softer cylinder insert and stiffer surrounding. Whereas Setup 2 has an even stiffer cylindrical part compared to Setup 1 but just as soft surrounding. Setup 4 is an inverse model of Setup 2 i.e. softer cylinder and stiffer surrounding.

Setup			
		Cylinder (Always SPIO-NP)	**Cuboid (Surrounding)**
Setup 1		4 freeze and thaw cycles	2 freeze and thaw cycles
Setup 2		8 freeze and thaw cycles	2 freeze and thaw cycles
Setup 3		2 freeze and thaw cycles	4 freeze and thaw cycles
Setup 4		2 freeze and thaw cycles	8 freeze and thaw cycles

Table 3: The arrangement of the freeze and thaw cycles for the two parts of the phantom. Four different setups were made.

The day before the experiments the two parts of the phantom were put together for one mutual freeze and thaw cycle. On the experiment day the phantoms were taken out from the freezer and put in the refrigerator for about two hours and then for about a half hour in room temperature to ensure that the phantoms were thoroughly thawed.

4.1.3 Elasticity Measurements

To determine the Young's modulus for 5 % PVA solution that had gone through two, four respectively eight freeze and thaw cycles an elasticity test was performed. In order to do these tests a scale, a stopwatch and a cylindrical object that could be lowered in steps with a resolution down to half a millimeter was needed, see figure 4 for the setup of the instruments. The trials were carried out on a cylindrical piece made out of 20 ml of 5 % PVA Solution, with a diameter of 44 mm. This piece was placed on the scale and directly beneath the lowering object that had a smaller diameter (21 mm) than the PVA cylinder. The scale was reset and the cylinder was lowered 0.5 mm into the PVA cylinder. Since PVA is a viscoelastic material a stopwatch was turned on and for every 20th second in two minutes the weight was noted. This was done to find after which point in time the scale had stabilized *i.e.* in a force/time plot the curved is horizontal. When two minutes had passed the object was lowered another 0.5 mm and the trial was repeated, this was repeated for every half a millimeter for total distance of 5.0 mm.
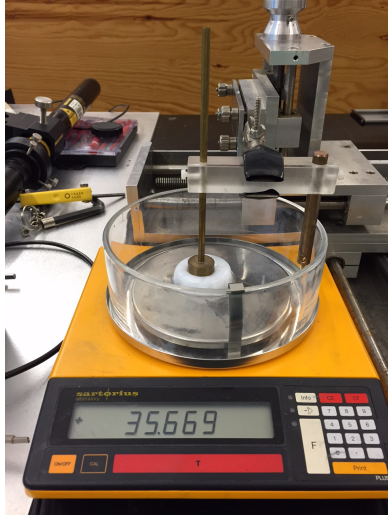
Figure 4: Setup for the elasticity measurements.

From the results of the elasticity measurements the Young's modulus, E, could be calculated using equation (12) (Sneddon, 1965);

$$E = mg \cdot \frac{(1 - \nu^2)}{D \cdot d} \tag{12}$$

where m is the weight noted of the scale, g is the gravitational constant, $9.82\ ms^{-2}$, ν is Poisson's ratio, 0.42, D is the diameter of the cylindrical lowering piece and d is the displacement.

4.1.4 Experimental Setup

To investigate the motion of the SPIO-NP within PVA with different stiffnesses, a MMUS system with an electro magnet containing an iron core and a solenoid, see figure 6(a) (in-house design, 7 kg copper wire, LTH, Lund, Sweden) and a high frequency ultrasound scanner, VisualSonics Vevo 2100, was used. A schematic diagram of the experimental setup can be seen in figure 5.
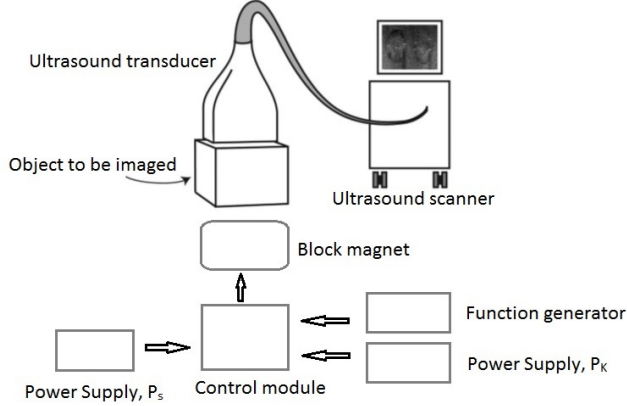
Figure 5: A schematic diagram of the experimental setup.

The phantom was taken out of its mold and placed on a thin piece of plastic on top of Plexiglas, see figure 6(b). On top of the phantom a layer of ultrasound gel was added to provide acoustic contact between the phantom and the transducer. The linear array transducer, MS250 was lowered down until it had contact with the surface of the phantom and a B-mode image was obtained. Underneath and as close as possible to the Plexiglas, the electro magnet was positioned to deliver the magnetic field to the phantom. To manipulate the magnetic field as desired, a power supply, P_K, (PSI 8080-60 T, Elektro-Automatik, Germany) was used to set the peak to peak voltage, V_{PP}, and a function generator (LFG-1310, Leader Electronics corp) was used to set the shape and frequency of the signal to the magnet. To obtain a square wave to excite the electro magnet a control module was used containing two capacitors, one heatsink and a control unit (in-house design, capacitors of 10 000 μF, LTH, Lund, Sweden). This control module was powered with a power supply, P_S, (EL302T, Thurlby Thandar Instruments Ltd., Huntingdon, United Kingdom).

<div align="center">(a)   (b)</div>
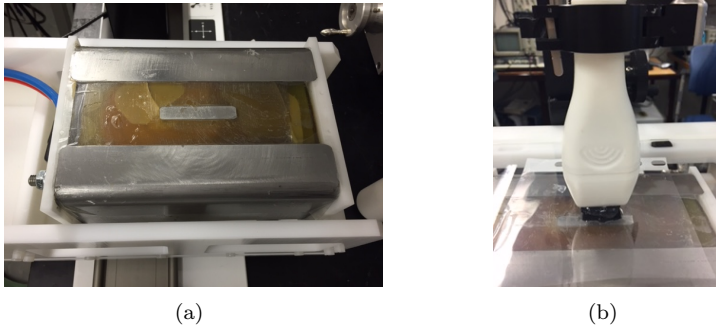
Figure 6: (a) The electro magnet used for the MMUS investigations (b) Setup of the ultrasound transducer, fantom and the electro magnet.

For each phantom investigation of the displacement of the SPIO-NP was performed with a square wave signal and with different frequencies around 2, 4 respectively 8 Hz and magnitudes of 10, 20 and 30 V_{PP}. The data from the ultrasound machine were collected and exported to Matlab (The MathWorks Inc., Natick, MA, USA) where the data was analyzed with the algorithm described in section 2.5.

4.2   Simulations in COMSOL 5.0

Comsol Multiphysics is a software tool based on advanced numerical methods for electrical, mechanical, fluid flow and chemical modeling and simulations (COMSOL, 2015). It is well suited for this project to simulate motion of magnetic nanoparticles distributed in a cancer mimicking tissue phantom that in turn is exposed to a magnetic field. A guide of the steps of how to build the model can be found in Appendix A. Also all dimensions and settings can be found there.

To simulate how a magnetic field affects the SPIO-NPs in different stiffnesses of PVA a numerical model was designed based on the experimental one. To design a numerical model in COMSOL, the built-in model wizard can be used which guides the user through the steps that is necessary for building a model. When these steps were done, the parameters that were needed for this model were set, see figure 30, in Appendix A. When all basic settings were made, it was time to start building the model. First a sphere was created with the purpose to wrap the whole geometry with the properties of air. The second part of the geometry was the solenoid that was build up with a cone-shaped iron core surrounded by a copper coil. Unfortunately differed the simulated magnet from the experimental one due to issues with the amplifier used for the experimental part. The third part was the phantom that is placed just above the tip of the core, see figure 7. Its dimensions corresponds to the experimental phantom. When the geometries were created, each was assigned with material properties. The properties of the phantom was varied depending on what was investigated, however what differs between the properties of the cylindrical hole of the phantom and the surrounding part of the phantom except from the investigations of the different stiffnesses were the SPIO-NP properties which were

<div align="center">20</div>

added to the properties of the cylindrical hole.
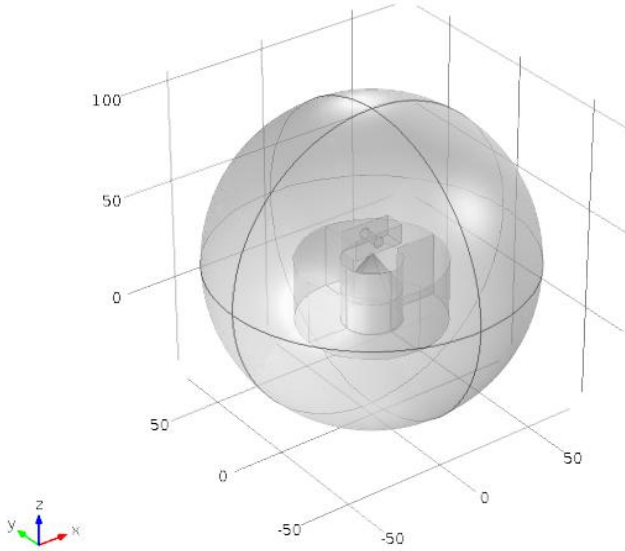
Figure 7: The geometry of the entire simulated region.

When the geometry and its material properties was added it was time to setup the three parts of the simulation i.e. the magnetic field, the partial differential equation and the solid mechanics. The magnetic field was modeled to simulate the magnetic field that is extending from the tip of the iron core. The solid mechanics was modeled to simulate the movement of the SPIO-NP within the cylinder using the force from the magnetic field as an input body load of the region with the SPIO-NP. The partial differential equation was added to calculate the gradient of the magnetic field along all axes which cannot be visualized directly in COMSOL. Before computing the three simulations, there was a need to mesh the geometry. Since the phantom was the main object, it was chosen a finer mesh for the phantom than for the surroundings, see figure 8.

21
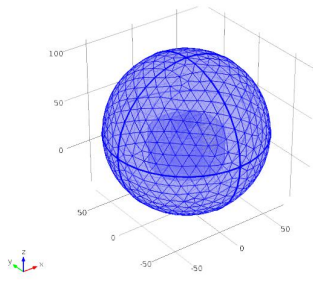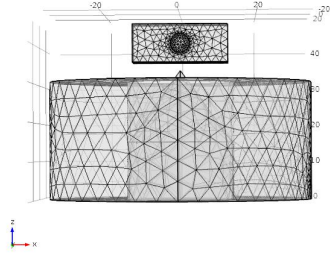
Figure 8: (a) The mesh for the hole phantom. (b) A close up of the mesh for the magnet and the phantom. Where a finer mesh of the phantom can be seen.

5 Results

This section shows the results obtained from the practical experiments and the COMSOL simulations.

5.1 Practical Experiments

Below are the results from the elasticity measurements as well as the MMUS measurements.

5.1.1 Elasticity Measurements

Figure 9 shows the force applied to the cylindrical PVA piece along the Y-axis, and the time on the X-axis. The curves imply that the scale stabilizes with time. Due to this, the Young's modulus, see equation (12), was calculated based on the values collected at 120 seconds.
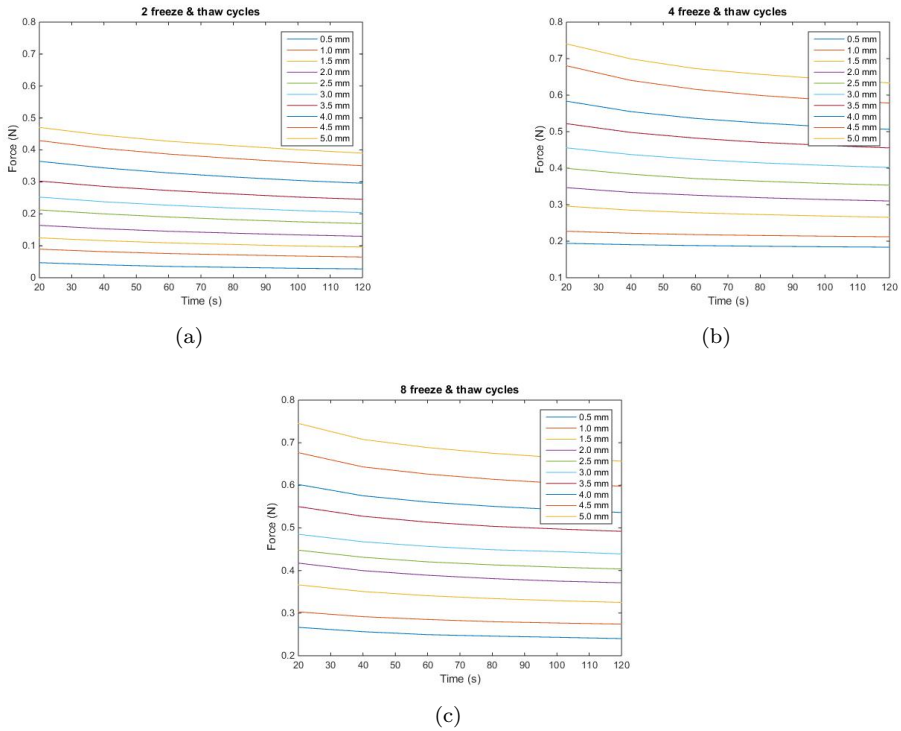
Figure 9: The relation between the measured force at a time interval of 120 seconds. (a) is for two freeze and thaw cycles and each curve represent respective displacement, (b) is for four freeze and thaw cycles and each curve represent respective displacement and (c) is for eight freeze and thaw cycles and each curve represent respective displacement.

The calculated mean Young's modulus for the three different freeze and thaw cycles can be seen in table 4.

Young's Modulus	
2 Freeze and thaw cycles	2.8 ± 0.1 kPa
4 Freeze and thaw cycles	5.3 ± 0.12 kPa
8 Freeze and thaw cycles	5.8 ± 0.24 kPa

Table 4: The results of the measured mean Young's modulus with two, four and eight freeze and thaw cycles.

5.1.2 Magnetomotive Ultrasound Measurements

The following images are obtained at an applied magnetic solenoid excitation frequency of 4 Hz and 30 V_{PP} with a NP-concentration of 0.3 mg Fe_3O_4/ml. The results from four different phantoms with different elastic properties are displayed. To see the results from the US measurements made with other frequencies and voltages see Appendix B.

Image (a) in the figures 10, 12, 14 and 16 shows the B-mode image of the phantom.

In image (b) in figures 10, 12, 14 and 16 the relative phase of the displacements is shown. It can be seen that the SPIO-NP-laden regions move with virtually the same phase. The surrounding region however moves with a π rad phase shift, i.e. the opposite phase. A transition is apparent, going from a distinct phase in the center of the insert and then gradually shifting π rad in the insert/surrounding interface. The regions above and below the SPIO-NP-laden cylinder moves in phase with the particles' displacements, thus giving the circle a more elongated shape in the z-direction. This effect is more apparent in the upper regions of the images.

Figures 11, 13, 15 and 17 show the total movement at all frequencies in (a). The movement at the right frequency, i.e. twice the excitation frequency, (8 Hz in this case) is color coded in (b). (c) shows the result of the phase-discriminating and frequency-tracked algorithm implemented on the collected MMUS data superimposed on top of the B-mode image. The color bar indicates the displacement magnitude in μm. The overall appearance of the (b) images indicate that the SPIO-NP laden cylindrical inserts move with virtually the same frequency as the surroundings although there are more movement inside and above the inserts. There seems to be no movement at all in the immediate region between the inserts and the surroundings, whereas the greatest movement occurs in the center of the insert slowly fading outwards.

The area showing displacement in 11(c) and 13(c) have a conical shape with slightly larger displacements in the area above the cylindrical insert, compared to 15(c) and 17(c) where the shape of the inserts are more apparent.

5.1.2.1 MMUS Results From Setup 1

Figures 10 and 11 display the results obtained from the US measurements on a phantom that has a stiff cylinder (4 freeze and thaw cycles) and a softer surrounding (2 freeze and thaw cycles) in accordance with setup 1, see table 3. 10(a) shows the B-mode image of the phantom. 10(b) shows the phase variation of the displacement across the B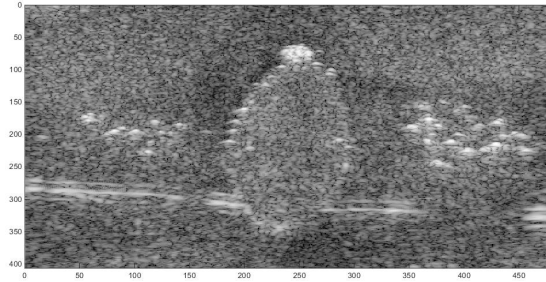-mode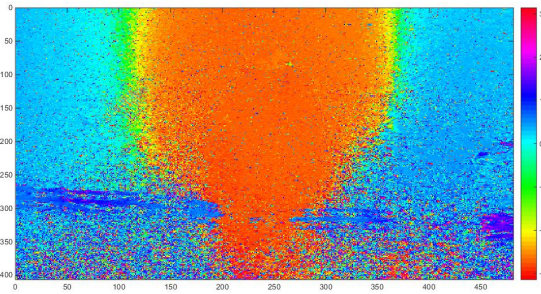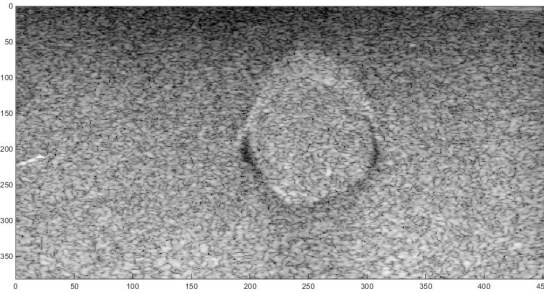 image where the color bar indicates the shift in radians. 11(a) shows the total movement at all frequencies, whereas 11(b) shows the movement only at the right frequency. 11(c) shows the magnitude of the displacements occurring at the right frequency and right phase. The color bar represents the displacement in μm.
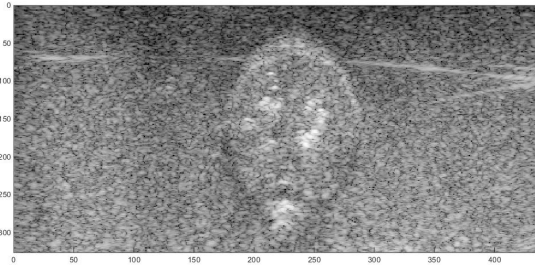
(a)
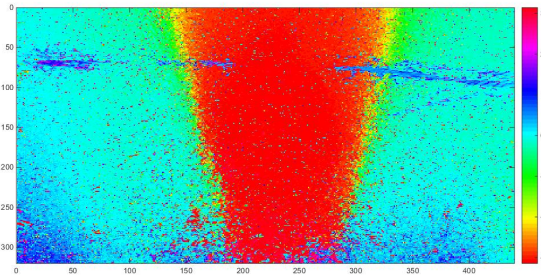
(b)

Figure 10: Result from setup 1. (a) B-mode image of the phantom. (b) Phase variation of the displacement across the B-mode image. The color bar indicates the phase shift in radians.
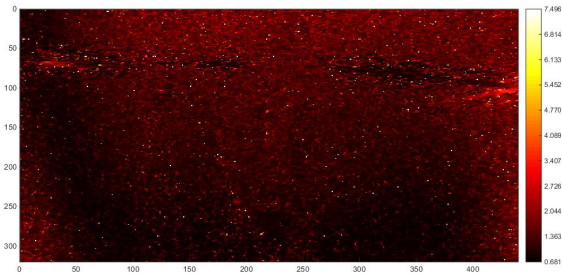
(a)
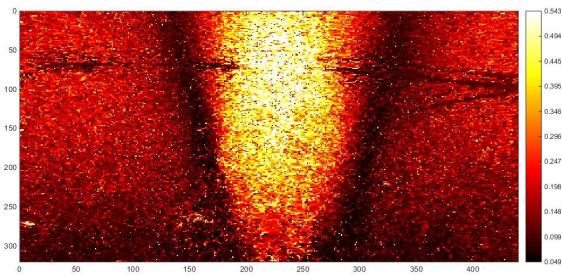
(b)
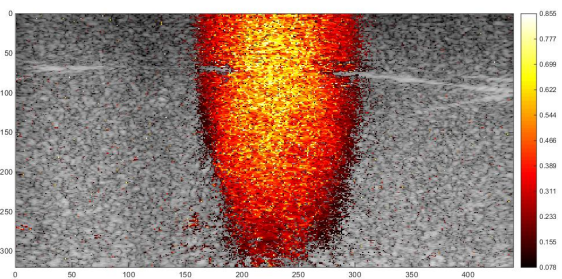
(c)

Figure 11: Result from setup 1. (a) Total movement at all frequencies. (b) Movement at the right frequency. (c) Magnitude of the displacements occurring at the right frequency and right phase. The color bar represents the displacement in μm.
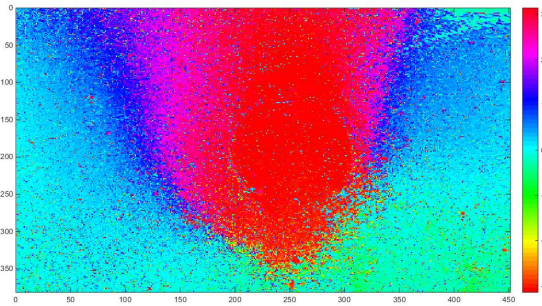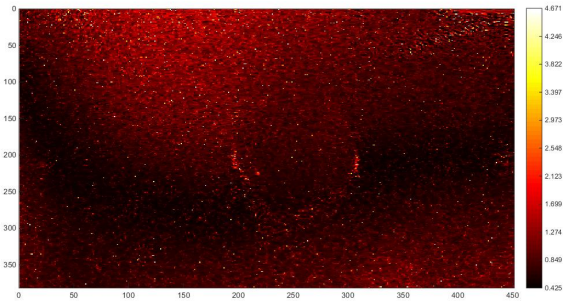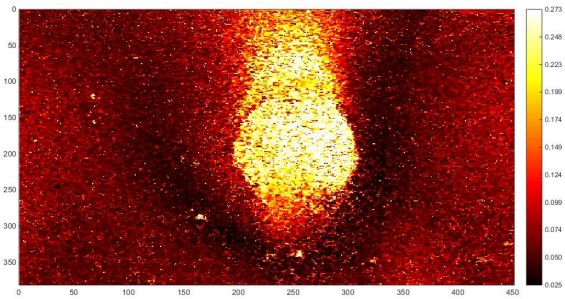
27

5.1.2.2   MMUS Results From Setup 2

Figures 12 and 13 display the results obtained from the US measurements on a phantom that has a stiff cylinder (8 freeze and thaw cycles) and a softer surrounding (2 freeze and thaw cycles) in accordance with setup 2, see table 3. 12(a) shows the B-mode image of the phantom. 12(b) shows the phase variation of the displacement across the B-mode image where the color bar indicates the shift in radians. 13(a) shows the total movement at all frequencies, whereas 13(b) shows the movement only at the right frequency. 13(c) shows the magnitude of the displacements occurring at the right frequency and right phase. The color bar represents the displacement in μm.
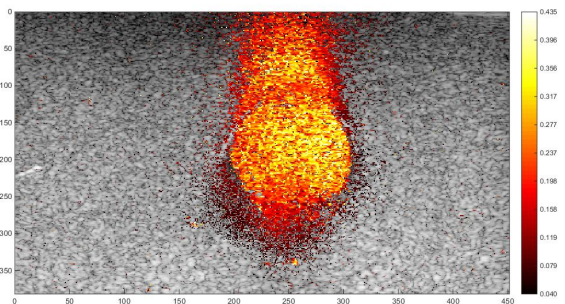

(a)

(b)

Figure 12: Result from setup 2. (a) B-mode image of the phantom. (b) Phase variation of the displacement across the B-mode image. The color bar indicates the phase shift in radians.
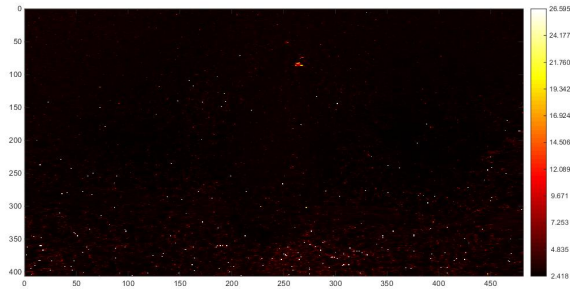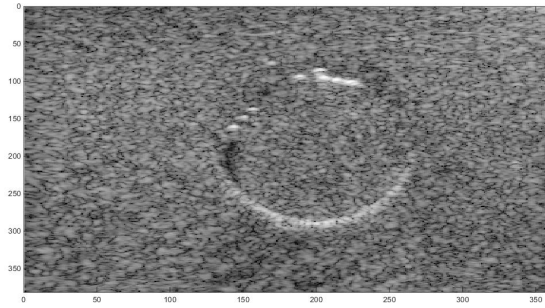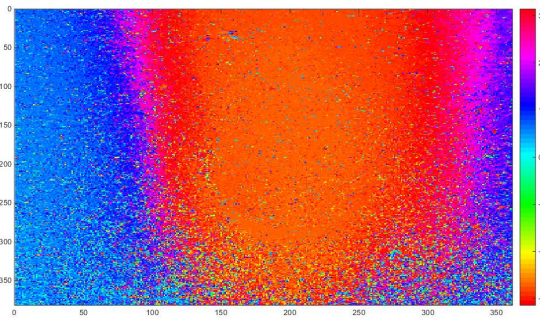
(a)
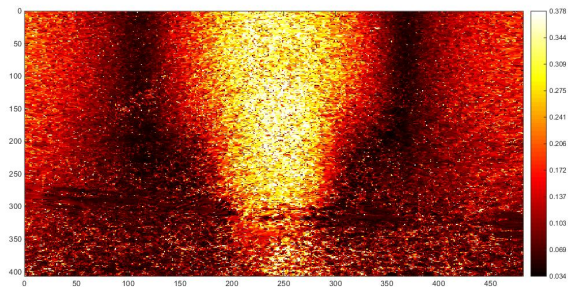
(b)
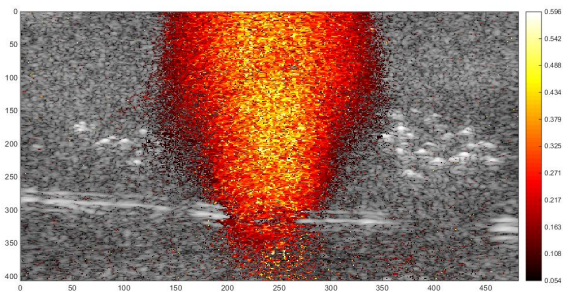
(c)

Figure 13: Result from setup 2. (a) Total movement at all frequencies. (b) Movement at the right frequency. (c) Magnitude of the displacements occurring at the right frequency and right phase. The color bar represents the displacement in μm.

5.1.2.3 MMUS Results From Setup 3

Figures 14 and 15 display the results obtained from the US measurements on a phantom that has a softer cylinder (2 freeze and thaw cycles) and a stiffer surrounding (4 freeze and thaw cycles) in accordance with setup 3, see table 3. 14(a) shows the B-mode image of the phantom. 14(b) shows the phase variation of the displacement across the B-mode image where the color bar indicates the shift in radians. 15(a) shows the total movement at all frequencies, whereas 15(b) shows the movement only at the right frequency. 15(c) shows the magnitude of the displacements occurring at the right frequency and right phase. The color bar represents the displacement in μm.


(a)

(b)

Figure 14: Result from setup 3. (a) B-mode image of the phantom. (b) Phase variation of the displacement across the B-mode image. The color bar indicates the phase shift in radians.
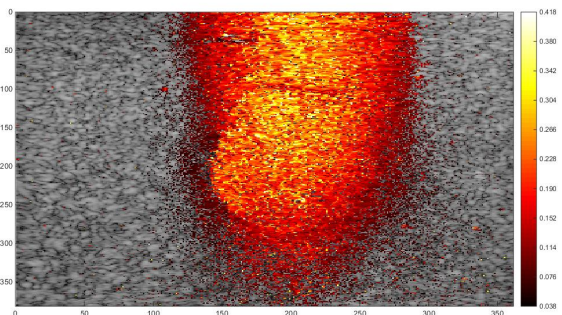
(a)

(b)

(c)

Figure 15: Result from setup 3. (a) Total movement at all frequencies. (b) Movement at the right frequency. (c) Magnitude of the displacements occurring at the right frequency and right phase. The color bar represents the displacement in μm.

5.1.2.4   MMUS Results From Setup 4

Figures 16 and 17 display the results obtained from the US measurements on a phantom that has a softer cylinder (2 freeze and thaw cycles) and a stiffer surrounding (8 freeze and thaw cycles) in accordance with setup 4, see table 3. 16(a) shows the B-mode image of the phantom. 16(b) shows the phase variation of the displacement across the B-mode image where the color bar indicates the shift in radians. 17(a) shows the total movement at all frequencies, whereas 17(b) shows the movement only at the right frequency. 17(c) shows the magnitude of the displacements occurring at the right frequency and right phase. The color bar represents the displacement in μm.

(a)

(b)

Figure 16: Result from setup 4. (a) B-mode image of the phantom. (b) Phase variation of the displacement across the B-mode image. The color bar indicates the phase shift in radians.
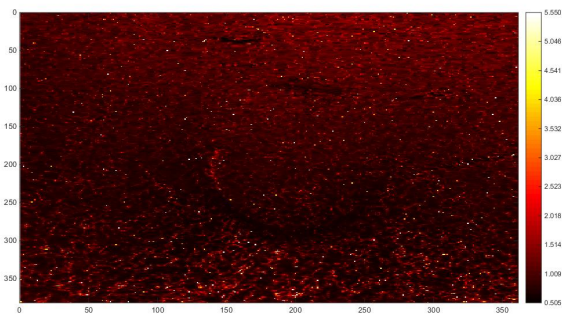
(a)
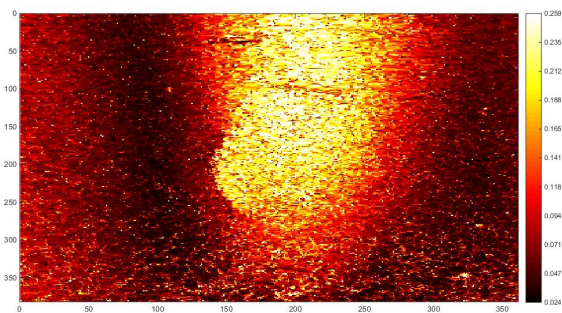
(b)

(c)

Figure 17: Result from setup 4. (a) Total movement at all frequencies. (b) Movement at the right frequency. (c) Magnitude of the displacements occurring at the right frequency and right phase. The color bar represents the displacement in μm.

5.2 Displacement Magnitude For Different Excitation Frequencies and Voltages

Figure 18 has a fixed frequency at 4 Hz and shows that with a higher voltage a greater displacement can be achieved. This is consistent for the four setups. As can be seen in figures 18(a) and 18(b) there is less displacement for setup 3 and 4 compared to setup 1 and 2. A greater displacement can be observed in the NP-laden inserts that has gone through 4 freeze and thaw cycles, compared to the one that has gone through 8 cycles, see figure 18(a). A relative motion reduction of 40, 20 and 30 % can be seen at 10, 20 and 30 V_{PP} in figure 18(a). For the two inverse cases, see figure 18(b) there is a relative motion reduction of 60, 30 and 20 % at 10, 20 and 30 V_{PP}

Figure 19 has a constant excitation voltage of 30 V_{PP} and shows that with higher frequencies the displacement will decrease. This is consistent for the four setups. As can be seen in figure 19(a) and 19(b) there is less displacement for setup 3 and 4 compared to setup 1 and 2. A greater displacement can be observed in the NP-laden inserts that has gone through 4 freeze and thaw cycles, compared to the one that had gone through 8 cycles, see figure 19(a). A relative motion reduction of 30, 30 and 20 % can be seen at 2, 4 and 8 Hz in figure 19(a). For the two inverse cases, see figure 19(b) there is a relative motion reduction of 20, 20 and 30 % at 2, 4 and 8 Hz.
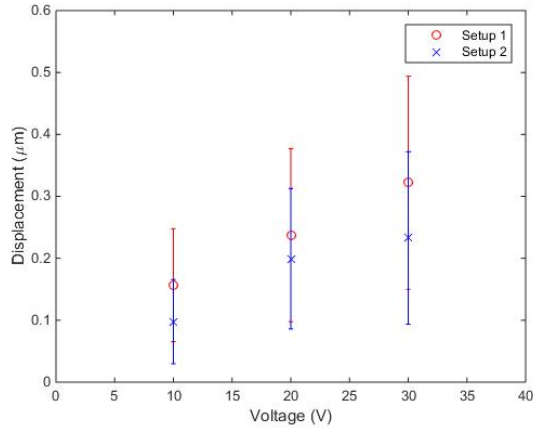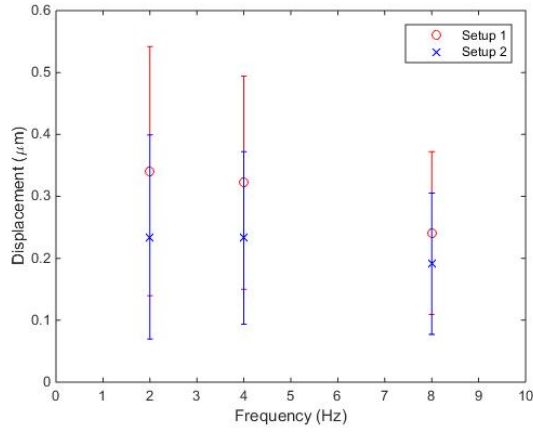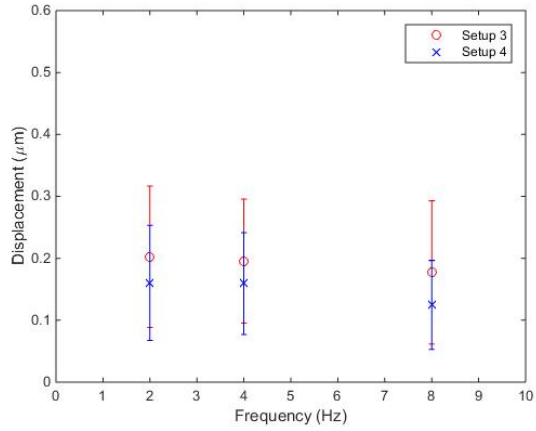
(a)
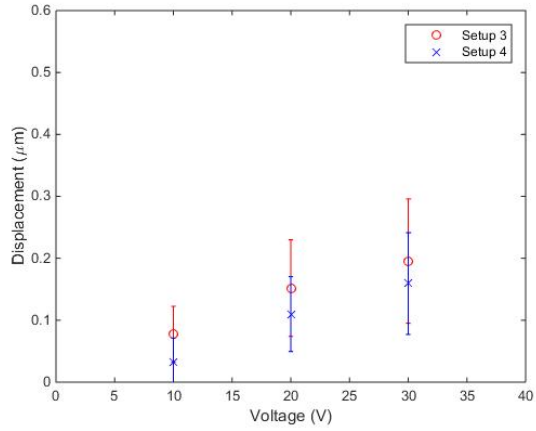
(b)

Figure 18: The relation between the displacement and applied solenoid voltage at a fixed frequency of 4 Hz. (a) The displacement for setup 1 and 2. (b) The displacement for setup 3 and 4.

(a)

(b)

Figure 19: The relation between the displacement and frequency at a fixed applied solenoid voltage of 30 V_{PP}. (a) The displacement for setup 1 and 2. (b) The displacement for setup 3 and 4.

5.3 Simulations in COMSOL 5.0

This section contains the results from the simulations made in COMSOL. Simulations are made based on the measured values in the experimental part of this report, as well as on values found in literature. The simulations made with theoretical values are performed to study quantitative behavior, whereas the simulations based on measured values are used to compare the simulated model to the real setup.

5.3.1 The Magnetic Field

Figure 20 shows the normalized magnetic flux density in the entire simulated region. Figure 21 shows the magnetic flux density in 3D. The magnetic field has almost no affection on the surrounding air, see equation (1), which is confirmed by the small almost not visible arrows in the figure, see figure 21. For the same reason the arrows are the largest in the immediate surroundings of the iron core. Arrows can also be seen in the phantom containing the magnetic nanoparticles, ensuring that the magnetic field is indeed affecting this area. A close-up of the phantom can be seen in figure 22. The figure suggests that the magnetic field is the strongest in the cylinder containing the magnetic particles. However, the result is slightly misleading since the equation used to calculate the field's distribution does not take account for the correct particle concentration. Rather, a much higher concentration is used which explains the magnitude of the field strength in the figure.
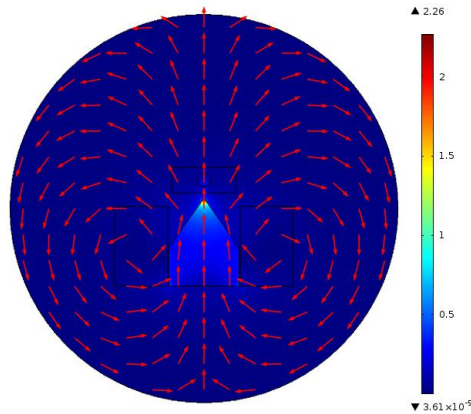

Figure 20: The normalized magnetic flux density. The color scale represents the magnetic flux density in Tesla.
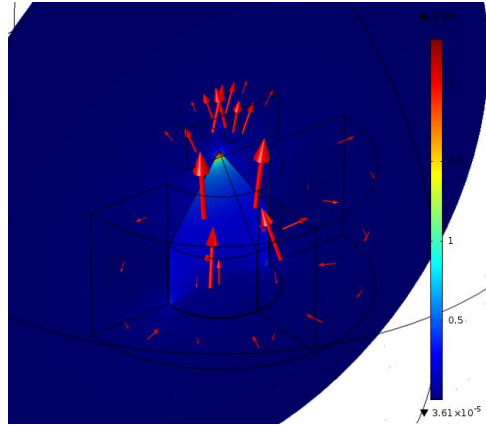
Figure 21: The magnetic flux density of the entire region. The color scale represents the magnetic flux density in Tesla.
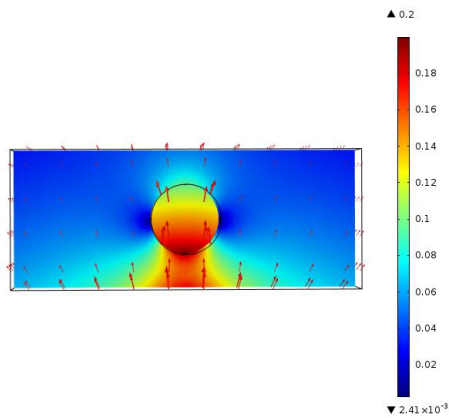

Figure 22: The magnetic flux density of the phantom. The color scale represents the magnetic flux density in Tesla.

5.3.2 The Displacement Magnitude

The following simulations are modeled in COMSOL based on a calculated magnetic field created by a solenoid with the current 60 A sent through a coil with 100 turns. The excitation frequency was set to 4 Hz. The arrows indicate the effect of the vertical and horizontal components of the displacement in a plane cut through the center of the phantom. Image (b) in the figures 23 to 25 are obtained at the same time, 0.65 s. This time point was chosen to display a distinct image of how the displacement moves in the vertical and horizontal direction. Image (a) in the same figures are obtained at the time, 0.19 s. This time point is the displacement magnitude maximum. The black triangle displayed on the bottom part of the figures represents the magnet. Each figure in this section has a corresponding result in the next section.

Some of the simulations are calculated based on the values obtained in the elasticity measurements in the practical part of this project, see section 5.1.1 and table 3, while others are made with values found in literature. The values for Poisson's ratio are based on values found in literature.

The overall result is that there is little or no visible difference in the simulation of the displacement field between regions with the same Young's modulus, see figure 61 and 62 in Appendix B.

The simulated version of the practical experiment, i.e. the Young's modulus set in COMSOL is based on the measured value from the elasticity measurements, see 5.1.1, shows that there is little to no difference in the displacement field when Young's modulus is within the same order of magnitude. The result can thereby be seen in figure 23. The rest of the results from the measured values of Young's modulus can be obtained in Appendix B. Figure 24 and figure 25 show the simulated displacement field for the case in which the elasticity values between the insert and the surrounding region are very large. Figure 24 has the stiffer region in the insert and figure 25 displays the inverted case. The values are based on elastic properties for different tissue types found in literature and are chosen to illustrate the greatest reasonable difference. Here, as expected, the two images display the greatest difference between them.
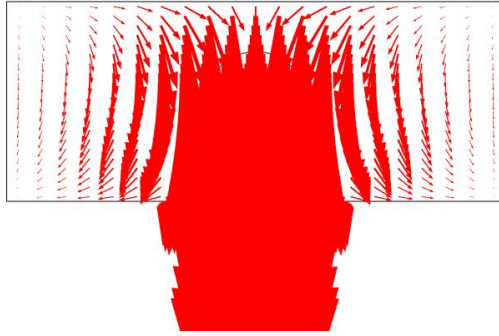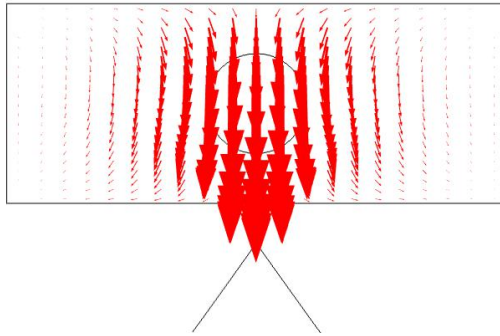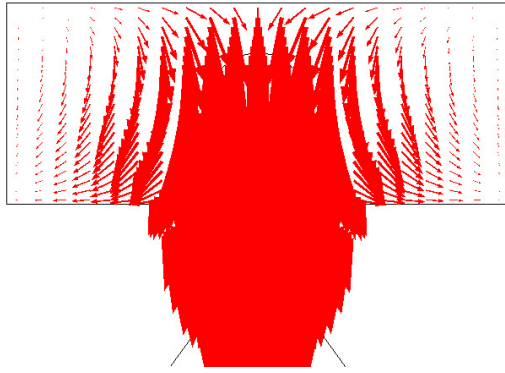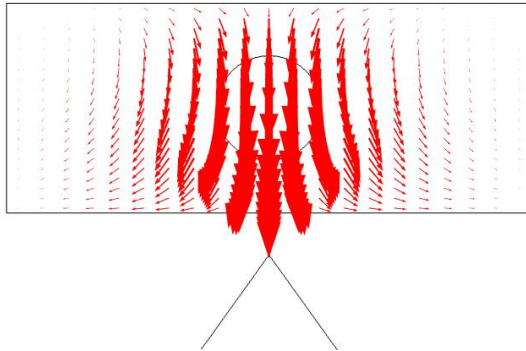
Figure 23: Displacement field for a phantom with an elastic property of $E = 2.8$ kPa and $\nu = 0.42$ for the surrounding and $E = 5.8$ kPa and $\nu = 0.42$ for the cylinder. (a) At a time where the maximum displacement is obtained. (b) At a time where the displacement in the phantom can be seen more clearly compared to the maximum displacement.
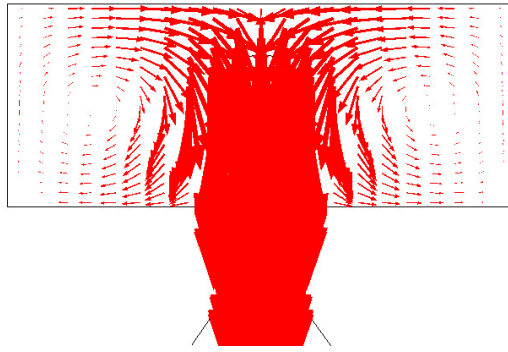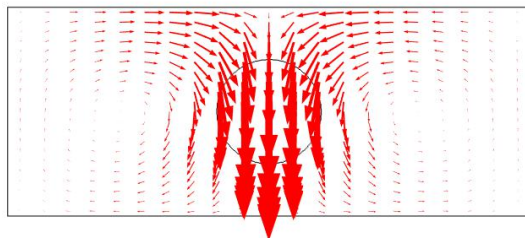
(a)

(b)

Figure 24: Displacement field for a phantom with an elastic property of $E = 21$ kPa and $\nu = 0.42$ for the surrounding and $E = 560$ kPa and $\nu = 0.42$ for the cylinder. (a) At a time where the maximum displacement is obtained. (b) At a time where the displacement in the phantom can be seen more clearly compared to the maximum displacement.

(a)

(b)

Figure 25: Displacement field for a phantom with an elastic property of $E = 560$ kPa and $\nu = 0.42$ for the surrounding and $E = 21$ kPa and $\nu = 0.42$ for the cylinder. (a) At a time where the maximum displacement is obtained. (b) At a time where the displacement in the phantom can be seen more clearly compared to the maximum displacement.

5.3.3 The Absolute Vertical Displacement Magnitude

As opposed to the previous section, these images show the result of the absolute displacement magnitude in the vertical direction only. This is the only direction in which a displacement can be detected by the US transducer, thus these images are comparable to the MMUS images. The color bar to the right indicates the displacement in mm. Once again the black triangular shape at the bottom of the figures represents the magnet. These results give a qualitative assessment of how the simulated magnetic field impacts a SPIO-NP-laden insert in a tissue mimicking phantom with regards to the induced movements. For each figure in this section, the corresponding displacement field in both vertical and horizontal direction can be visualized in the previous section.

Some of the simulations are calculated based on the values obtained in the elasticity measurements in the practical part of this project, see section 5.1.1 and table 3, while others are made with values found in literature. The values for Poisson's ratio are solely based on values found in literature.

The images show little to no visible difference in the displacement field between the regions with the same Young's modulus, see figure 61(b) and 62(b) in Appendix B. The same goes for the simulated version of the practical experiment, i.e. the Young's modulus set in COMSOL is based on the measured value from the elasticity measurements, see 5.1.1. The result can thereby be seen in figure 26. The rest of the results from the measured values of Young's modulus can be obtained in Appendix B.

Figure 27 and 28 simulate the biggest difference between the insert and the surrounding region and are therefore expected to stand out, in the same way as in the previous section.
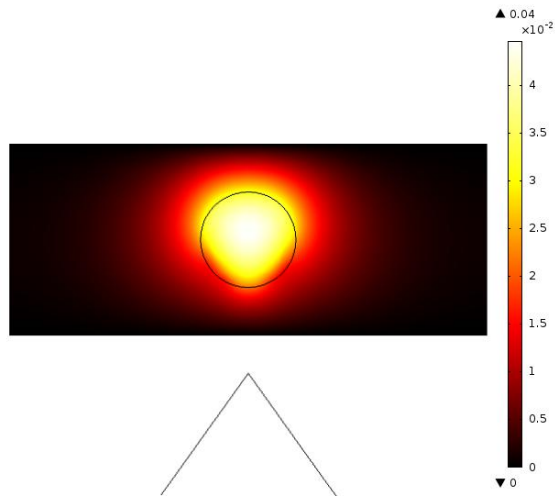
Figure 26: Absolute displacement in the vertical direction for a phantom with elastic properties corresponding to setup 2, i.e. Young's modulus is set to $E = 2.8$ kPa outside the cylindrical insert, and $E = 5.8$ kPa inside. Poisson's ratio is set to $\nu = 0.42$ for both regions.
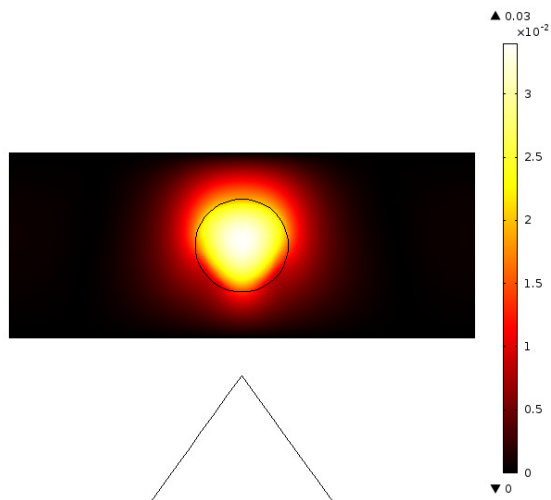

Figure 27: Absolute displacement in the vertical direction for a phantom with Young's modulus set to $E = 560$ kPa inside the insert and $E = 21$ kPa outside. Poisson's ratio is set to $\nu = 0.42$ for both regions.
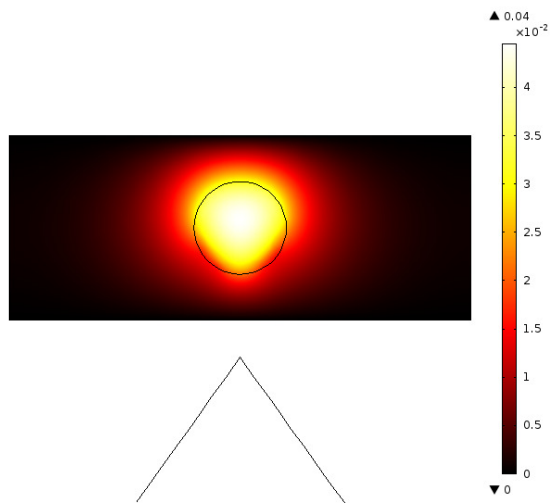
44

Figure 28: Absolute displacement in the vertical direction for a phantom with Young's modulus set to $E = 21$ kPa inside the insert and $E = 560$ kPa outside. Poisson's ratio is set to $\nu = 0.42$ for both regions.

5.3.4 The Simulated Relation Between The Displacement and Young's Modulus

Figure 29 shows an evident difference between a phantom with a stiffer inner region compared to a phantom with a stiffer outer region. Both cases indicate a distinct reduction of the displacement for higher Young's modulii. It can also be seen that with a higher Young's modulus a significant difference of the displacement occurs between the stiffer inner region and the stiffer outer region. The softer region in both cases was fixed at 1.5 kPa. As can be seen in figure 29, the relative difference of the displacement is only about 4 %, even when the change in Young's modulus is tenfold.
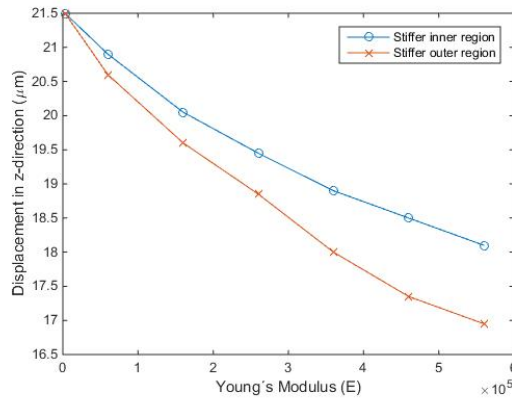

Figure 29: The simulated relation between the displacement and Young's modulus for a stiffer inner region (blue curve) and for a stiffer outer region (red curve). Starting at a Young's modulus set to $E = 2.8$ kPa and Poisson's ratio set to $\nu = 0.42$ and ending at a Young's modulus set to $E = 560$ kPa and Poisson's ratio set to $\nu = 0.43$. For each Young's modulus that was higher than 2.8 kPa the Poisson's ratio was set to 0.43.

6 Discussion

The measured mean Young's modulus increases with the number of freeze and thaw cycles, see table 4. This corresponds with behavior confirmed in previous studies (Duboeuf et al., 2007) (Fromageau et al., 2003). However, the values calculated in this trial are considerably smaller than the ones calculated by for example Duboeuf *et al* (2007). We believe this is due to a number of reasons, the first and possibly the foremost being that the concentration of PVA differs, from 5 % in our experiments compared to 10 % or higher in the other experiments we have come across. The ability to control and monitor the temperature during the freeze and thaw cycle was also non existing in our trials, and therefore the impact this may have had on the polymer bindings occurring in the solidification process could not be determined.

Poisson's ratio for PVA, also used in the above mentioned equation, is only assumed, based on values given in various studies performed by for example Fromageau *et al* (2003), and further reduces the credibility of our calculated values. However, since the influence of the PVA concentration on the elastic properties has not yet, to our knowledge, been firmly established, our values may not be that far from the reality. Despite them being lower than perhaps expected, their behavior with respect to freeze and thaw cycles acts in consistency with those produced by others that have performed more accurate measurements.

Thus, we believe that the viscoelastic properties that the PVA phantom exhibits, requires a far more elaborate approach in order to obtain a trustworthy estimate of the Young's modulus than that performed in this report. It is also highly likely that the equations used here do not hold in the viscoelastic region. Regardless of whether or not the measured values of Young's modulus for the 5 % PVA phantom is an absolute reflection of the real values, they most certainly display the sought feature of increasing its stiffness with the number of freeze and thaw cycles.

Our US images show that by applying a time-varying sinusoidal magnetic field a motion was induced in the SPIO-NP-laden regions and their surroundings as expected. This induced motion caused displacements on the μm scale and could be detected by performing the phase-gated and frequency discriminating algorithm, see section 2.5, on the collected US data.

Since no measurements were made on phantoms not containing magnetic NP's, we cannot debate the origin of the π rad shift observed in all images, but merely confirm that it exists and corresponds to previous results made by others. However, this effect cannot be observed in our simulations and we believe this to be an effect of the boundary conditions made in the model. For future work it would be interesting to study the behavior of the transition of this π radian shift in the phantoms. This transition is more abrupt in setup 3 and 4.

The conical shape observed in the images is explained by the propagation of the ultrasound wave, which only detects motion in the vertical direction. Thus, the movement in other directions will not be apparent in the images. As the induced

motion in the bottom part of the phantom will push underlying regions aside in the horizontal axis, this displacement will not show up in the images despite being there. This is further explained by the bottom part of the phantom being fixed at the glass table, acting as a rigid wall, whereas the other phantom parts, with the air or US gel interface, can have movement in the horizontal directions.

We see in figures 18 and 19 that there is an overall difference in the displacement magnitude when the elastic properties differs between the insert and the surrounding region, which confirms our hypothesis. Our results indicate that stiffer regions, whether being surrounded by softer regions or surrounding softer regions, will result in a smaller displacement magnitude. As equation (5) indicated, the total force acting on the SPIO-NP's will decrease with stiffness, as is confirmed in figures 18(a) and 19(a). The insert that underwent 4 freeze and thaw cycles induces a greater displacement than the same version for 8 cycles in agreement with the previous mentioned equation. However, as figures 18(b) and 19(b) shows, we see that the displacement magnitude is overall smaller for the phantoms with the softest insert. This contradicts our previous reasoning but we argue that this is due to the surrounding area being stiffer in this case, counteracting the magnetic insert's effort to induce movement. This effect can be observed in figure 15(c) and 17(c) where the softer insert is more distinct in shape, and more so in the 4 cycle case compared to 8.

We saw no effect of the threshold observed by both (Evertsson et al., 2013) and (Jansson et al., 2014) in our experiments and believe that this is a result of the magnet used in this report being sufficiently stronger. However, in figure 18(a) there seems to be some sort of an "anti" threshold when extrapolating, *i.e.* a state for which zero applied voltage still would induce a movement in the tissue for setup 1. Also, for setup 2, 3 and 4 a threshold effect is implied by the gradient of the curves.

As can be seen in figure 29, the COMSOL model confirms the measured result that the displacement magnitude decreases with stiffnes, *i.e.* Young's modulus. However the simulated model suggests displacements far larger than observed in our experiments. We believe this to be the consequence of two things:

The mean displacement calculated from our obtained MMUS images is based on the average movement of the entire particle laden region. However, there is a risk, although very unlikely, that the distribution of magnetic NP's is uneven in the cylinder, a consequence of the particle sedimenting in the cylinder during the making of the phantoms. If this is the case, the mean value for the displacement could be misleadingly low, considering the MMUS image is obtained at a cross-section approxiamtely in the center of the cylinder. The COMSOL model takes no account for this uneven distribution and calculates the mean displacement in a point in the center of the cylinder, as if this point was equally surrounded by nanoparticles in each direction. The other factor influencing the results in the model are the values for Young's modulus. We have assumed in the simulations that our measured values are correct, however as discussed earlier they may be slightly off.

7 Conclusions

We draw the conclusion that the model used in this project is an excellent tool for qualitative assessments. However, to be used as a quantitative tool for high precision investigations it needs further development. For investigating extreme situations however, *i.e.* cases when extremely large and/or small values are compared, it is excellent.

We have in this report shown that by using magnetomotive ultrasound imaging in conjunction with magnetic nanoparticles, a difference in elastic properties in tissue can be detected. This has been shown both by experiments and by simulating the events in a finite element method based software.

A more effective and accurate method for determining the elastic properties for the phantom material is required if practical experiments are to be performed. The method used for this project is far too inaccurate and time consuming to be used in a larger scale research.

To further evaluate the possibilities for the conclusions drawn in this report to be utilized clinically however, more studies are needed. More insight on the elastic properties of cancerous tissue is required, and a more elaborate model of the lymph node needs to be designed in the simulation.
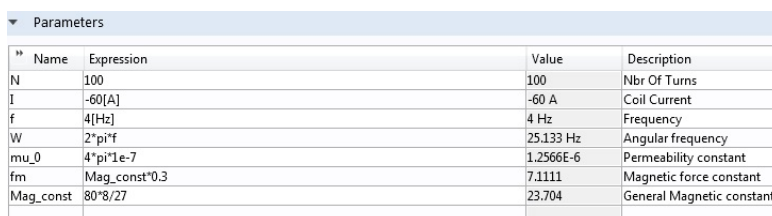
A Appendix

The following section is a manual on how to build the model used in this report from scratch.

Manual to COMSOL 5.0

Start up

1. Create a new **Model Wizard**.

2. Select the *Space Dimensions* to **3D**.

3. Select Physics: $AC/DC \rightarrow$ add **Magnetic Fields (mf)** $\rightarrow$ Press *Study* to continue.

4. Select *Study* $\rightarrow$ **Stationary** $\rightarrow$ Press Done.

5. Under *Component 1* $\rightarrow$ *Geometry 1* $\rightarrow$ Under *Units* change the *Length unit* to **mm**.

6. Next step is to add parameters. Under *Global* $\rightarrow$ *Definitions*, right click and select **Parameters**. Under *Parameters* add the parameters that you need, see figure 30.

▼ Parameters			
» Name	Expression	Value	Description
N	100	100	Nbr Of Turns
I	-60[A]	-60 A	Coil Current
f	4[Hz]	4 Hz	Frequency
W	2*pi*f	25.133 Hz	Angular frequency
mu_0	4*pi*1e-7	1.2566E-6	Permeability constant
fm	Mag_const*0.3	7.1111	Magnetic force constant
Mag_const	80*8/27	23.704	General Magnetic constant

Figure 30: The parameters that are needed in the model.

The Geometry

1. The first part to build is a sphere that will surround the whole geometry, including all the other parts. To build this right click on *Geometry 1* and add the **Sphere**. Click on the *Sphere 1* to set its measurements, see figure 31, and then finish by clicking on *Build Selected*.

2. Next step is to make the iron core for the magnet. To build this a cylinder and a cone is needed. Start by right clicking on *Geometry 1* and add the **Cylinder**. Click on *Cylinder 1* to set its measurements, see figure 32 and then finish by clicking on *Build Selected*. Then right click again on *Geometry 1* to add the **Cone**. Click on *Cone 1* to set its measurements, see figure 33. Finish by clicking on *Build Selected*.
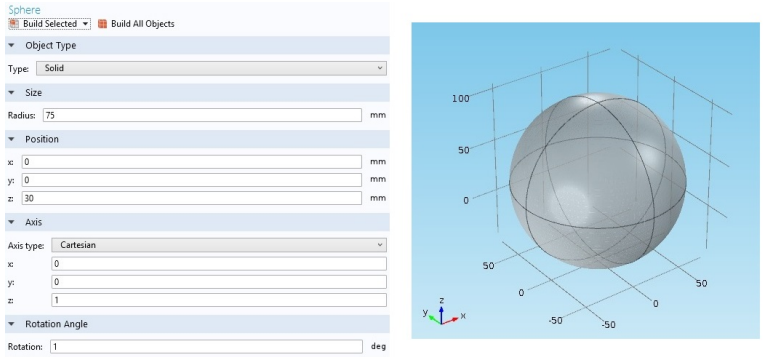
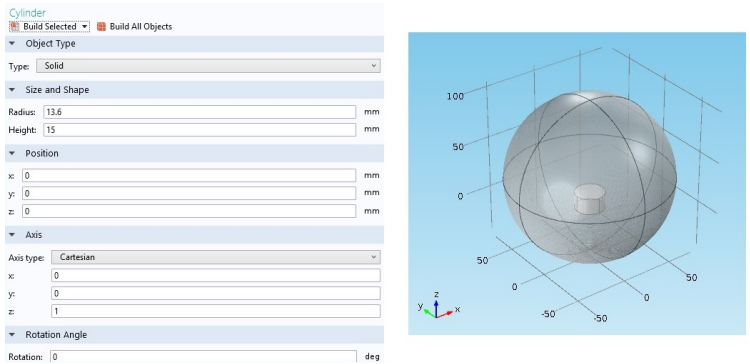Figure 31: The size and measurements of the sphere.

Figure 32: The cylinder for the iron core and its measurements.

To make the iron core function as one whole geometry, a union between the cylinder and the cone needs to be made. Right click on *Geometry 1 → Booleans and Partitions →* **Union**. Under *Union 1* select the cylinder and cone and uncheck *Keep interior boundaries*. Finish by clicking on *Build Selected*.

3. To create the Copper coil wrapped around the iron core right click on *Geometry 1* and add a **Work Plane**. Under *Work Plane 1 → Plane Definition* set the *plane* to **zx-plane**. Right click on *Plane Geometry* under *Work Plane 1* and select the **Rectangle**. Set the rectangle's measurements, see figure 34. Finish by clicking on *Build Selected*.

When all settings are done right click again on *Work Plane 1* and select **Revolve**. Under *Revolve 1 → Revolution Axis → Directions of revolution axis* set the *xw* to **1** and *yw* to **0** and then finish by click on *Build Selected*.

4. Next step is to create the phantom. Right click on *Geometry 1* and select a **Block**. Click on *Block 1* and set the measurements as seen in figure 35 and then finish by clicking on *Build Selected*. Then right click again on *Geometry*
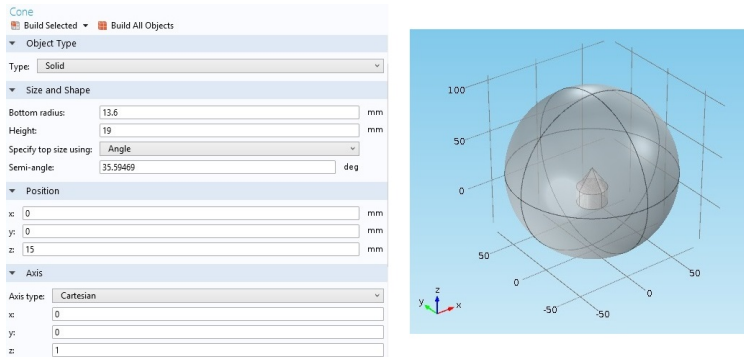
Figure 33: The cone for the iron core and its measurements.

1 and this time select a **Cylinder**. To set the measurements of the cylinder click on *Cylinder 2*, see figure 36. Finish by clicking on *Build selected*.
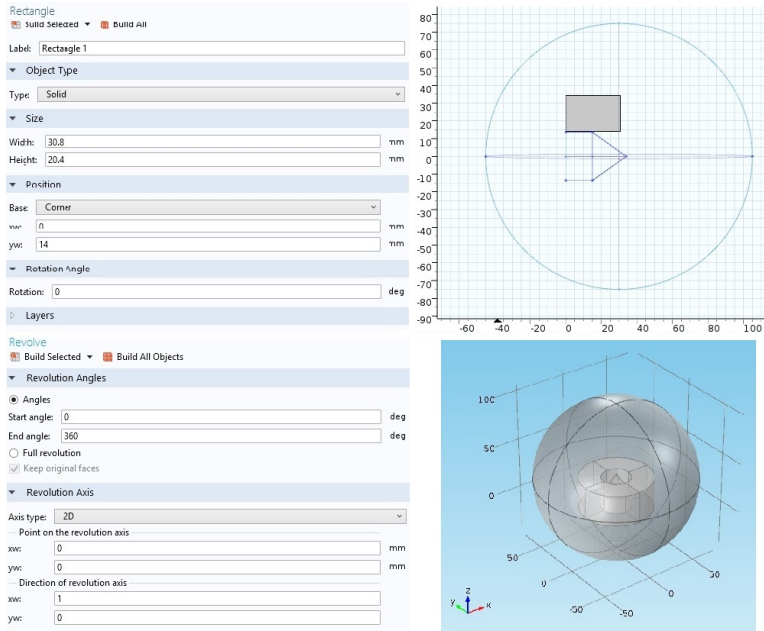
Figure 34: The settings and measurements for the coil.
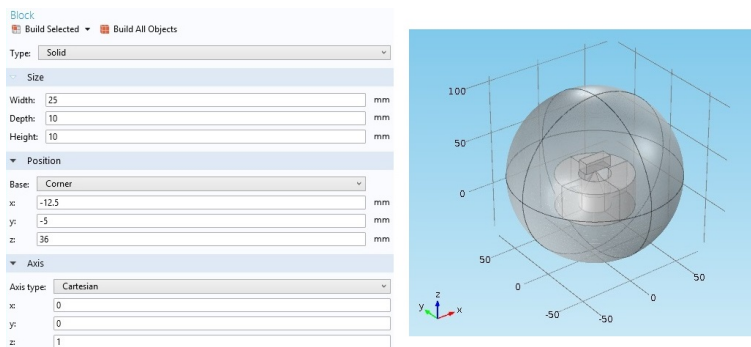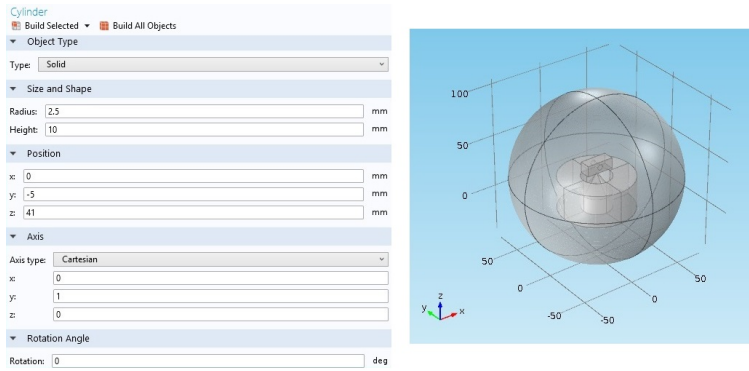

Figure 35: The measurements for the phantom block.

Figure 36: The measurements for the cylinder inn the phantom.

5. When all geometries are made finish by click on *Build All Objects*.

Materials

In this section the materials are defined and linked to the respective geometry.

1. The first step is adding all the materials to Component 1. Right click on *Materials* under *Component 1* and **Add Material**. This will open a menu and under the tab *built in* the materials **air, copper** and **iron** can be found. Add these materials to *Component 1*. The materials for the phantom needs to be added manually and when added they can be found under the tab *User-Defined Library*. To add your own material right click on *Materials* and click on **Blank Material**. A tap of *Material X* will show up under *Materials*, click on it and change the *Label* to a more suited name. To add the material properties go in under *Material Properties* and find all properties that are needed.

   For PVA (representing tissue) add the properties that can be seen in figure 37.

	Property	Name	Value	Unit	Property group
✓	Density	rho	1215	kg/m³	Basic
✓	Electrical conductivity	sigma	1.25e-15	S/m	Basic
✓	Relative permeability	mur	1	1	Basic
✓	Relative permittivity	epsilonr	1	1	Basic
✓	Bulk modulus	K	0.28e9	N/m²	Bulk modulus and shear m...
✓	Shear modulus	G	10e5	N/m²	Bulk modulus and shear m...
	Poisson's ratio	nu	0.459	1	Basic
	Young's modulus	E	1000	Pa	Basic
	Shear modulus	Gv	10e5	N/m²	Linear viscoelastic material
	Bulk modulus	K	0.28e9	N/m²	Linear viscoelastic material

Figure 37: This table shows the values needed for adding the PVA to the material library.

For PVA with iron properties (representing tissue with nanoparticles) add the properties that can be seen in figure 38.

	Property	Name	Value	Unit	Property group
✓	Density	rho	1215	kg/m³	Basic
✓	Electrical conductivity	sigma	1.25e-15	S/m	Basic
✓	Relative permeability	mur	1	1	Basic
✓	Relative permittivity	epsilonr	1	1	Basic
✓	Bulk modulus	K	0.28e9	N/m²	Bulk modulus and shear m...
✓	Shear modulus	G	10e5	N/m²	Bulk modulus and shear m...
	Poisson's ratio	nu	0.459	1	Basic
	Young's modulus	E	1000	Pa	Basic
	Shear modulus	Gv	10e5	N/m²	Linear viscoelastic material
	Bulk modulus	K	0.28e9	N/m²	Linear viscoelastic material

Figure 38: This table shows the values needed for adding the PVA with nanoparticles to the material library.

To save your own added materials to the User-Defined Library right click on *Material X* and *Add to User-Defined Library*.

The final step is to match the materials to the right geometry. Click on each material and select the domain that should have the material property. Air – Sphere, Copper – Coil, Iron – Core, PVA – Block, PVA (Cancer tissue with nano particles) – Cylinder.

Magnetic Fields

The magnetic field interface was added with the Model wizard and by default it adds difference nodes such as Ampère's Law, Magnetic Insulation and Initial Values. To be able to run the simulation additional nodes and boundary conditions are necessary.

1. These nodes can be added by right clicking on *Magnetic Fields* and adding the **Multi-Turn Coil**. Under *Multi-Turn Coil 1* select the domain that represent the Coil and select the *Coil Type* to be **Circular**. Under *Multi-Turn Coil* change the *Number of turns* to be **N**, the *Coil current* to be **I** and the *Coil name* to **Coil**. Also change the *Material type* under *Material Type* to **From material**.

2. Next step is to add the reference edge, right click on *Multi-Turn Coil 1* → *Edges* → add the **Reference Edge**. Under *Reference Edge 1* you can define the direction in which the current is flowing, select the coils inner edges to do this, see figure 39.

3. Under *Magnetic Fields* → *Ampère's Law 1* → *Material Type* → change the *Material type* to **From material**.
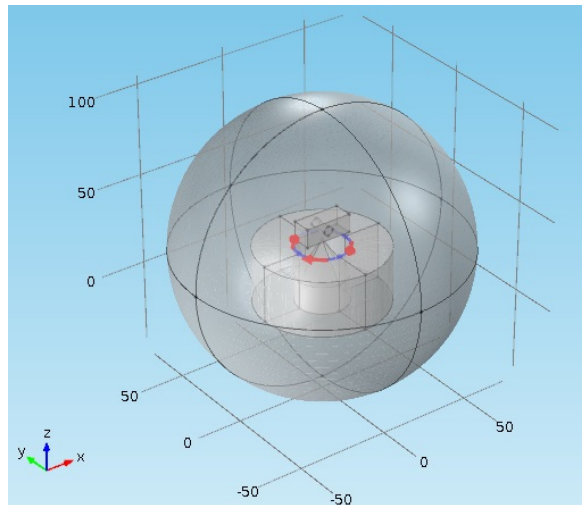
Figure 39: This picture shows how the reference edge is defined.

Partial Differential Equations

To calculate the magnetic field gradient the partial differential equations (PDE's) need to be added.

1. To do this right click on *Component 1 → Add Physics*. This will open a menu where you can find the PDE under *Mathematics → PDE Interface →* add **Coefficient form PDE**. In the *Coefficient From PDE (c) → Units* change the *Dependent variable quantity and Source term quantity* to **Magnetic flux density (T)** and under *Dependent Variables* change the *Number of dependent variables* to **3** and the *Dependent variable u* to **u1** just for esthetic's reasons.

   Go in under *Coefficient form PDE 1*

   → *Diffusion Coefficient* and set *c* to a **zero matrix**.

   → *Absorption Coefficient* and set *a* to the **unit matrix**.

   → *Source Term* and set *f* to **mf.Bx, mf.By, mf.Bz**.

   → *Damping or Mass Coefficient* and set d_a to a **zero matrix**.

   Under *Coefficient Form PDE (c) → Initial Values 1*, change the *Initial Values* for *u1* to **mf.Bx**, *u2* to **mf.By** and *u3* to **mf.Bz**.

Solid Mechanics

1. To add the Solid Mechanics physics interface right click on *Component 1 → Add Physics* to open the physics menu. In the menu click on *Structural Mechanics* and add the **Solid Mechanics**.

   Under *Solid Mechanics* select the domains for the Block and Cylinder and change the *Equation form* to **Time dependent** under *Equation*. Also change *Displacement field* under *Dependent Variables* to **u4**.

2. Under *Solid Mechanics → Linear Elastic Material 1 → Linear Elastic Material* check in **Nearly incompressible material** and change the *Specify* to **Bulk modulus and shear modulus**.

3. Right click on *Linear Elastic Material 1* and add **Viscoelasticity**, under *Viscoelasticity 1 → Viscoelasticity Model* change the *Shear modulus* to **10e5[Pa]** and the *Relaxation time* to **12[s]**.

4. To add a body load, right click on *Solid Mechanics → Volume Forces* and add **Body Load**. Under *Body Load 1* add the cylinder domain and add the equations under *Force*, see figure 40.

5. Next step is to add a roller, right click on *Solid Mechanics* and add **Roller**. Under *Roller 1* select the phantom's boundaries except for the mantle of the cylinder.

6. Right click on *Solid Mechanics* and add **Free**, in *Free 2* select the boundaries for the mantle of the cylinder.
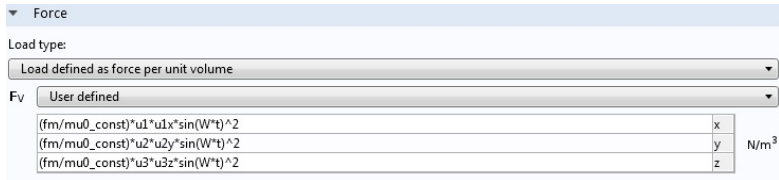
Figure 40: The equations that need to be added when adding the body load.

Mesh

1. To do the mesh click on *Mesh 1* and change the *Sequence type* under *Mesh Settings* to **User-controlled mesh**. You can change the element size under *Mesh 1* → *Size* → *Element Size* → change *Predefined* to **Fine**. Then under *Mesh 1* → *Free Tetrahedral 1* → *Domain Selection* select **Domain** and under *Selection* select **All domains**. Right click on *Free Tetrahedral 1* under *Mesh 1* and add **Size**, then go in under *Size 1* and add the **block** and **cylinder** to the *Geometric Entity Selection*. Then under Element Size change the *Predefined* to **Extra fine**.

2. When all settings are done, click on *Build All* to do the mesh.
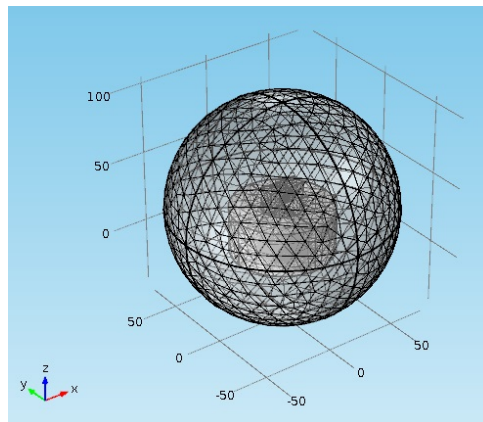
Figure 41: This picture shows the mesh when it is computed.

Study

1. For this experiment you need at least 3 study types, the first one is already existing and is *Study 1* that is stationary. Next you have to add Study 2 and 3, to do this right click on *ManualToComsol5.mph* and **Add Study**. The menu *Add Study* will now appear. Here you will select the study type. First select one additionally **Stationary** and for the second one select the **Time Dependent**.

2. When *Study 2* and *Study 3* is added, go to *Study 1* and under *Study Settings* uncheck **Generate default plot**. When this is done go to *Step 1: Stationary* under *Study 1* and check in **Plot** under *Results While Solving*. Under *Physics and Variables Selection* deselect **Coefficient From PDE (c)** and **Solid Mechanics (solid)**. Next right click on *Study 1* and select **Show Default Solver**.

3. Go to *Study 2* and under *Study Settings* unclick **Generate default plot**. When this is done go to *Step 1: Stationary* under *Study 2* and under *Physics and Variables Selection* deselect **Magnetic Fields (mf)** and **Solid Mechanics (solid)**. Then under *Values of Dependent Variables* check in *Values of variables not solved for* and under
→ *Method* select **Solution**.
→ *Study* select **Study 1, Stationary** then uncheck *Values of variables not solved for*.

Right click on *Study 2* and select **Show Default Solver**.

4. Go to *Study 3* and under *Study Settings* unclick **Generate default plot**. When this is done go to *Step 1: Time Dependent* under *Study 3*. Under *Study Settings* set the *Times* to **range(0,0.01,1)** and then under *Physics and Variables Selection* deselect **Magnetic Fields (mf)** and **Coefficient From PDE (c)**. Under *Values of Dependent Variables* → check in *Values of variables not solved for* and the under *Method* select **Solution** and under *Study* select **Study 2, Stationary**. Right click on *Study 3* and select **Show Default Solver**. Under *Study 3* → *Solver Configurations* → *Solution 3* → *Dependent Variables 1* → *Auxiliary pressure (comp1.solid.pw)* → under *Scaling* change the *Method* to **Manual** and *Scale* to **100000000**.

Results

Next step is to form the visualization of the result.

1. Go in under *Results* and right click on *Data Sets* and add **Solution**, do this 3 times. Then go in under each solution and change each *Label*. The names should be **Study 1/Solution 1, Study 1/Magnetic Phantom, Study 2/Solution 1, Study 2/Solution 2, Study 3/Solution 1, Study 3/SolidMech Phantom**

2. Right click on *Data Sets* under *Result* and add **3 Cut Plane** and one **Cut Point 3D**. For two of the *Cut plan*, change their *Label* to **Cut Plane Phantom SolidMech** and **Cut Plane Phantom SolidOrt**.

3. Go in under *Result* → *Data Sets*

Under *Study 1/Solution 1* → *Solution* → change the *Solution* to **Solution 1**.
Under *Study 2/Solution 2* → *Solution* → change the *Solution* to **Solution 2**.
Under *Study 3/Solution 1* → *Solution* → change the *Solution* to **Solution 3**.

4. Under *Results* → *Data Sets*
Right click on *Study 2/Solution 2* and add **Selection**. Go then in under

Selection and add the **cylinder domain**.

Right click on *Study 1/Magnetic Phantom* and add **Selection**. Go then in under *Selection* and add the **cylinder and block domains**.

Right click on *Study 3/SolidMech Phantom* and add **Selection**. Go then in under *Selection* and add the **cylinder and block domains**. Also uncheck **Propagate to lower dimensions**.

5. Under *Cut Plane 1 → Data →* change the *Data Set* to **Study 1/Solution 1** and under *Plane Data → Plane* to **XZ-planes**.

   Under *Cut Point 3D 1 → Data →* change the *Data Set* to **Study 3/Solution 1** and under *Point Data* set the *X* and *Y* to **0** and *Z* to **41**.

   Under *Study 3/SolidMech Phantom → Solution →* change the *Solution* to **Solution 3**.

   Under *Cut Plane Phantom SolidMech → Data →* change the *Data Set* to **Study 3/SolidMech Phantom** and under *Plane Data → Plane* to **XZ-planes**.

   Under *Cut Plane Phantom SolidOrt → Data →* change the *Data Set* to **Study 3/SolidMech Phantom**.

6. Right click on *Result* and add a **2D Plot Group**. Go under *Results → 2D Plot Group 1* and change the *Label* to **2D B-field with arrows**. Under *Data → Data set* select *Cut Plane 1* and under *Plot Settings → Plot data set edges* set the *Frame* to **Material**.

7. Next right click on *2D B-field with arrows* and add **Arrow Surface** and **Surface**. Under *Arrow Surface 1 → Expression* set the *x component* to **mf.Bx** and the *y component* to **mf.Bz**. Under *Coloring and Style* change *Arrow length* to **Normalized** and *Scale factor* to **11.65749**. Then under *2D B-field with arrows → Surface 1* set the *Expression* to **mf.normB** and the *Unit* to **T**.

8. Right click on *Results* and add **3D Plot Group**, under *3D Plot Group X* change the *Label* to **Magnetic Flux Density Norm (mf)** and then right click on *Magnetic Flux Density Norm (mf) → More Plots* and add **Multislice**. Right click again on *Magnetic Flux Density Norm (mf)* and add **Arrow Surface**.

   Under *Magnetic Flux Density Norm (mf) → Data → Data set* select **Study 1/Solution 1**.

   Under *Magnetic Flux Density Norm (mf) → Multislice 1 → Multiplane Data → X-planes* set *Planes* to **0**.

   → *Y-planes* set *Planes* to **1**.

   → *Z-planes* set *Planes* to **0**.

   Under *Magnetic Flux Density Norm (mf) → Arrow Surface* change the *Expression → X component* to **mf.BX**, *Y component* to **mf.BY** and *Z component* to **mf.BZ**.

9. Right click on *Results* and add **3D Plot Group**, under *3D Plot Group X* change the *Label* to **3D Plot B-field Magnetic** and change *Data set* under *Data* to **Study 2/Solution 1**. Then right click on *3D Plot B-field Magnetic → More Plots* and add **Multislice**. Go in under *Multislice 1 → Expression* and change the *Expression* to **mf.Bz** and *Multislice 1 → Multiplane Data*

$\rightarrow$ *X-planes* set *Planes* to **0**.
$\rightarrow$ *Y-planes* set *Planes* to **1**.
$\rightarrow$ *Z-planes* set *Planes* to **1**.

10. Right click on *Results* and add **3D Plot Group**, under *3D Plot Group X* change the *Label* to **3D Plot B-field PDE** and change *Data set* under *Data* to **Study 2/Solution 1**. Then right click on *3D Plot B-field PDE* $\rightarrow$ *More Plots* and add **Multislice**. Go in under *Multislice 1* $\rightarrow$ *Expression* and change the *Expression* to **u3** and *Multislice 1* $\rightarrow$ *Multiplane Data*
$\rightarrow$ *X-planes* set *Planes* to **0**.
$\rightarrow$ *Y-planes* set *Planes* to **1**.
$\rightarrow$ *Z-planes* set *Planes* to **1**.

11. Right click on *Results* and add **3D Plot Group**, under *3D Plot Group X* change the *Label* to **3D Plot Group**. Then right click on *3D Plot Group* and add **Slice**.

12. Right click on *Results* and add **3D Plot Group**, under *3D Plot Group X* change the *Label* to **Stress (solid)** and change *Data set* under *Data* to **Cut Plane Phantom SolidMech**. Right click on *Stress (Solid)* and add *Slice 1*. Then under *Slice 1*
$\rightarrow$ *Data* select *Data set* to **Study 3/SolidMech Phantom**.
$\rightarrow$ *Expression* $\rightarrow$ change the *Expression* to **abs(w4)**.
$\rightarrow$ change the *Unit* to **mm**.
$\rightarrow$ *Plane Data* set *Plane* to **ZX-planes** and *Planes* to **1**.
$\rightarrow$ *Coloring and Style* change the *Color table* to **Thermal**.
$\rightarrow$ *Quality* set *Resolution* to **Fine** and *Smoothing* to **Everywhere**.
$\rightarrow$ *Inherit Style* uncheck *Deform scale factor*.

13. Right click on *Results* and add **2D Plot Group**, under *2D Plot Group X* change the *Label* to **2D Plot Z-Displacement** and change *Data set* under *Data* to **Cut Plane Phantom SolidMech**. Then right click on *2D Plot Z-Displacement* and add **Surface**. Under *2D Plot Z-Displacement* $\rightarrow$ *Surface 1*
$\rightarrow$ *Data* select *Data set* to **Cut Plane Phantom SolidMech**.
$\rightarrow$ *Expression* $\rightarrow$ change the *Expression* to **abs(w4)** and the *Unit* to **mm**.
Then under *Surface* $\rightarrow$ *Coloring and Style* change the *Color table* to **ThermalEquidistant**.

14. Right click on *Results* and add **2D Plot Group**, under *2D Plot Group X* change the *Label* to **2D Plot Arrows InterInserts** and change *Data set* under *Data* to **Cut Plane Phantom SolidMech**. Then right click on *2D Plot Arrows InterInserts* and add **Arrow Surface**. Under *2D Plot Arrows InterInserts* $\rightarrow$ *Arrow Surface 1*
$\rightarrow$ *Expression* $\rightarrow$ change the *x component* to **u4** and *y component* to **w4**.
$\rightarrow$ *Arrow Positioning* $\rightarrow$ set *Points* under *x grid points* to **21** and under *y grid points* to **21**.
$\rightarrow$ *Coloring and Style* $\rightarrow$ check in *Scale factor* and set it to **500**.

15. Right click on *Results* and add **2D Plot Group**, under *2D Plot Group X* change the *Label* to **2D Plot Arrows IntraInsert** and change *Data set* under

Data to **Cut Plane Phantom SolidOrt**. Then right click on *2D Plot Arrows IntraInsert* and add **Arrow Surface**. Under *2D Plot Arrows IntraInsert →* *Arrow Surface 1*

→ *Expression* → change the *x component* to **v4** and *y component* to **w4**.
→ *Arrow Positioning* set *Points* under *x grid points* to **9** and under *y grid points* to **9**.
→ *Coloring and Style* → check in *Scale factor* and set it to **500**.

16. Right click on *Results* and add **1D Plot Group**, under *1D Plot Group X* change the lable to **1D Plot Group**. Change *Data set* to **Cut Point3D 1**. Under *Plot Settings* set *x-axis label* to **Time (s)** and *y-axis label* to **Displacement field, Z component (mm)**. Under *Axis* set *x minimum* to **-0.009999990463256836**, *x maximum* to **1.0099999904632568**, *y minimum* to **-0.00824572704732418** and *y maximum* to **6.273093167692423E-4**.

17. Right click on *1D Plot Group* under *Results* and add **Point Graph**. Click on *Point Graph* and under *Data* change *Data set* to **Cut Point 3D 1**. Under *y-Axis Data* change *Expressin* to **w4** and *Unit* to **mm**. Under *x-axis Data* change *Parameter* to **Time** and *Unit* to **s**.

18. Under *Study 1 → Step 1: Stationary → Results while Solving →* change *Plot group* to **3D Plot B-field Magnetic**.

19. Under *Study 2 → Step 1: Stationary → Results while Solving →* change *Plot group* to **3D Plot B-field Magnetic**.

20. Under *Study 3 → Step 1: Stationary → Results while Solving →* change *Plot group* to **3D Plot B-field Magnetic**.

B   Appendix

Magnetomotive Ultrasound Images

This section contains images obtained from the MMUS measurements. For setup explanations see table 3. For each image the magnitude of the displacement for the correct frequency, i.e. twice the solenoid excitation frequency see equation (4), and phase is displayed across the corresponding B-mode image. The color bar indicates the displacement magnitude in μm.

Setup 1
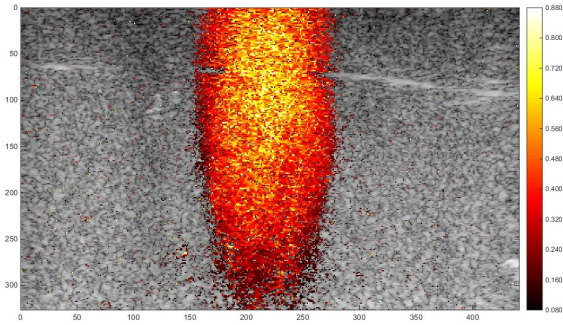
(a)
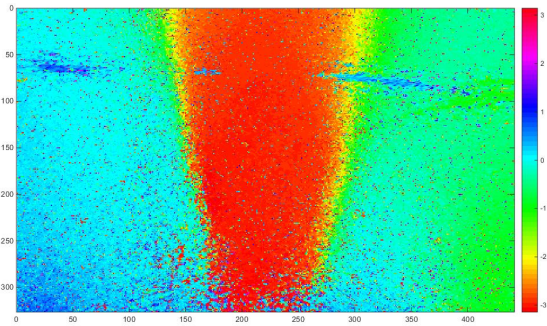
(b)

Figure 42: Images obtained at solenoid excitation frequency 2 Hz and 30 V_{PP}. The mean displacement within the cylinder is 0.3189 ± 0.2022 μm. (a) Magnitude of the displacements occurring at the right frequency and right phase. The color bar represents the displacement in μm. (b) Phase variation of the displacement across the B-mode image. The color bar indicates the phase shift in radians.
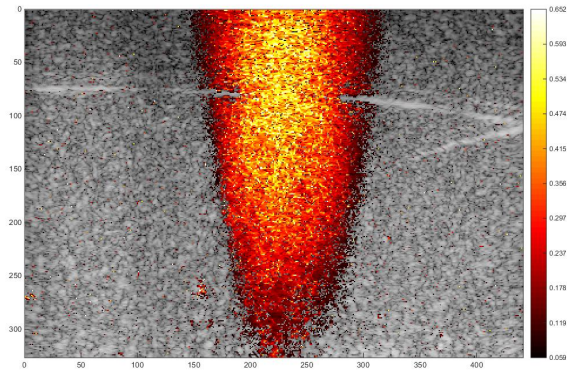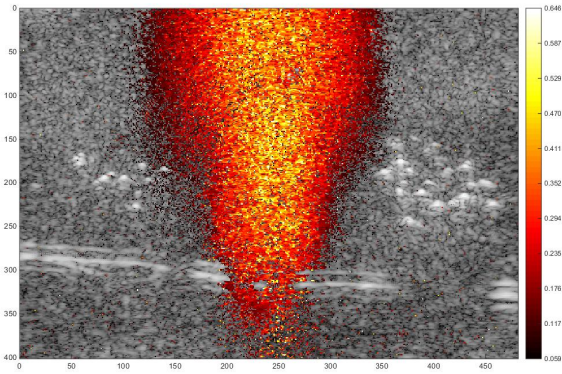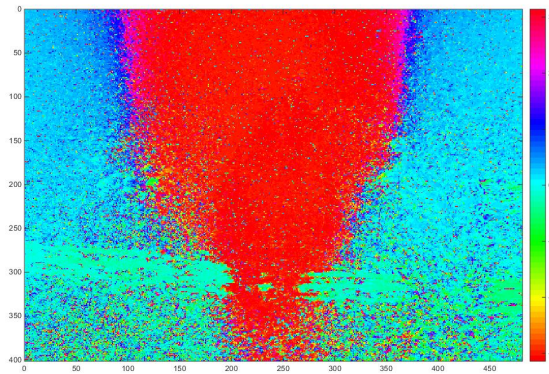
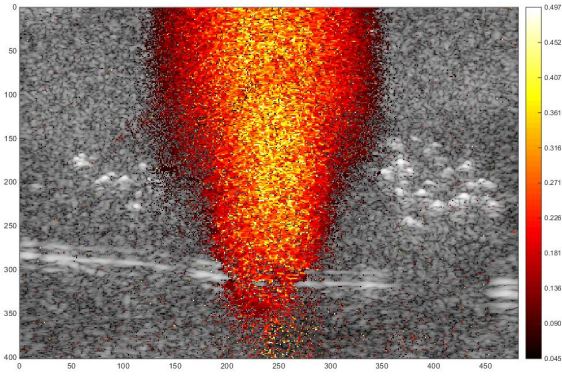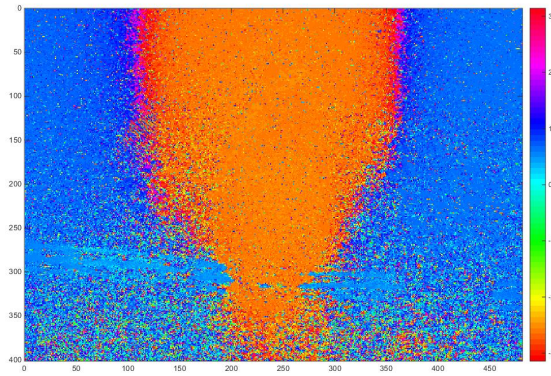(a)
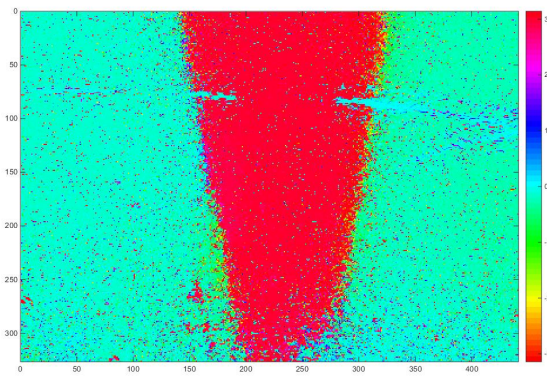
(b)

Figure 43: Image obtained at solenoid excitation frequency 8 Hz and 30 V_{PP}. The mean displacement within the cylinder is 0.2355 ± 0.1324 μm. (a) Magnitude of the displacements occurring at the right frequency and right phase. The color bar represents the displacement in μm. (b) Phase variation of the displacement across the B-mode image. The color bar indicates the phase shift in radians.
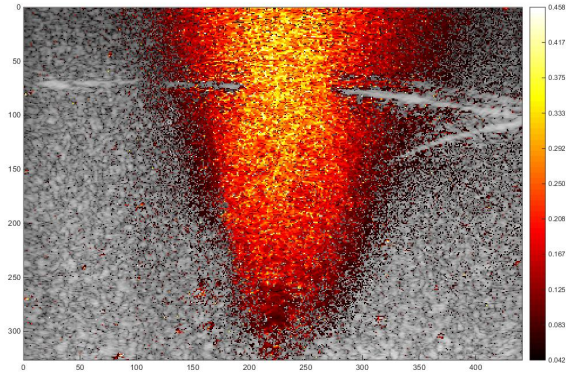
(a)
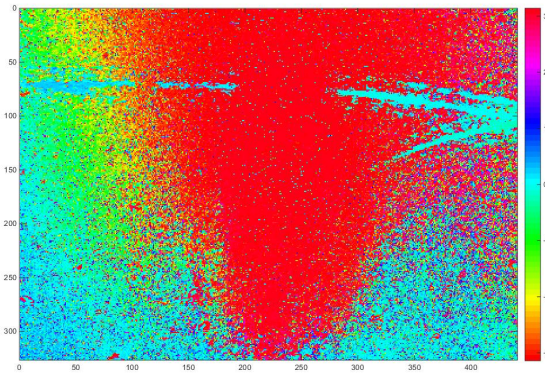
(b)

Figure 44: Image obtained at solenoid excitation frequency 4 Hz and 10 V_{PP}. The mean displacement within the cylinder is 0.1578 ± 0.0913 μm. (a) Magnitude of the displacements occurring at the right frequency and right phase. The color bar represents the displacement in μm. (b) Phase variation of the displacement across the B-mode image. The color bar indicates the phase shift in radians.
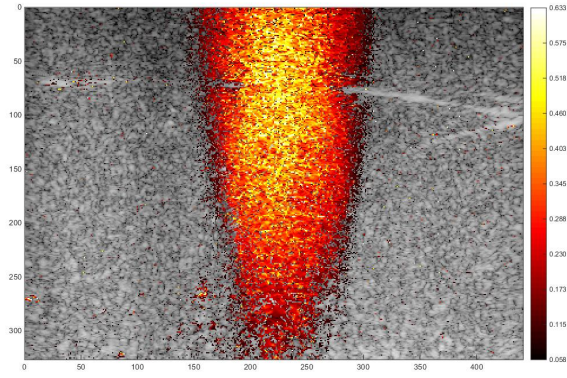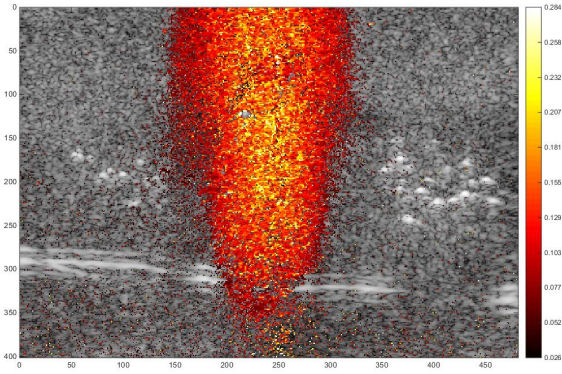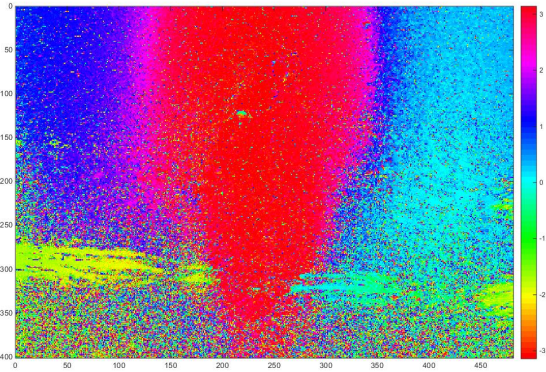
(a)
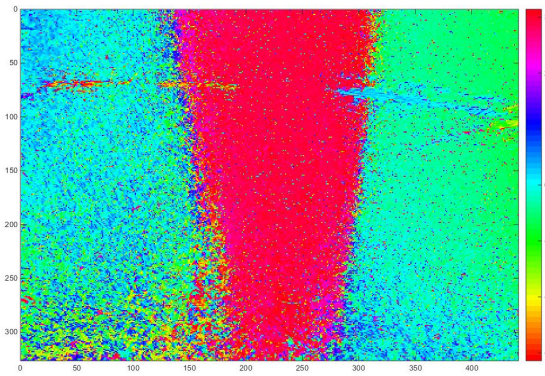
(b)

Figure 45: Image obtained at solenoid excitation frequency 4 Hz and 20 V_{PP}. The mean displacement within the cylinder is 0.2336 ± 0.1360 μm. (a) Magnitude of the displacements occurring at the right frequency and right phase. The color bar represents the displacement in μm. (b) Phase variation of the displacement across the B-mode image. The color bar indicates the phase shift in radians.

Setup 2

(a)

(b)

Figure 46: Image obtained at solenoid excitation frequency 2 Hz and 30 V_{PP}. The mean displacement within the cylinder is 0.2358 ± 0.1640 μm. (a) Magnitude of the displacements occurring at the right frequency and right phase. The color bar represents the displacement in μm. (b) Phase variation of the displacement across the B-mode image. The color bar indicates the phase shift in radians.
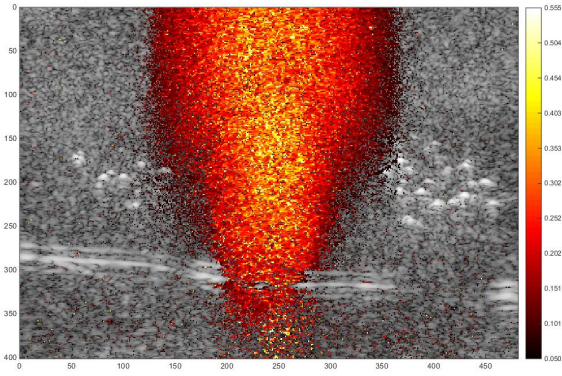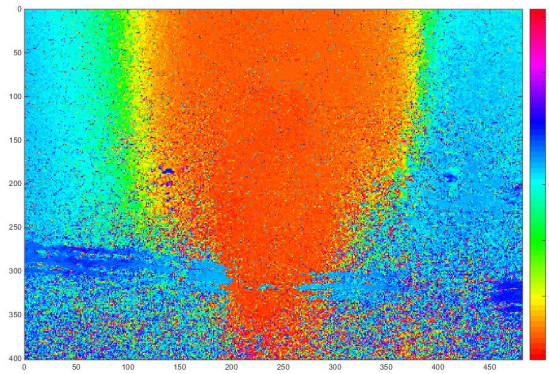
(a)

(b)

Figure 47: Image obtained at solenoid excitation frequency 8 Hz and 30 V_{PP}. The mean displacement within the cylinder is 0.1863 ± 0.1159 μm. (a) Magnitude of the displacements occurring at the right frequency and right phase. The color bar represents the displacement in μm. (b) Phase variation of the displacement across the B-mode image. The color bar indicates the phase shift in radians.
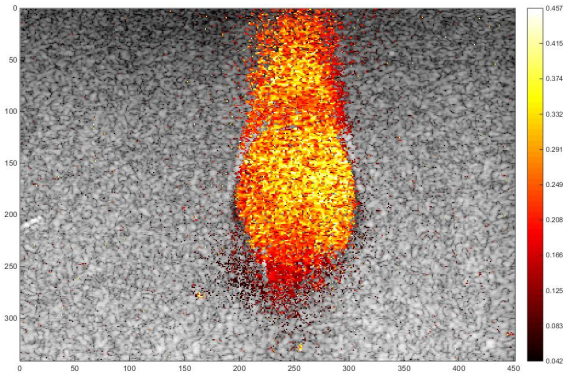
(a)

(b)

Figure 48: Image obtained at solenoid excitation frequency 4 Hz and 10 V_{PP}. The mean displacement within the cylinder is 0.0897 ± 0.0683 μm. (a) Magnitude of the displacements occurring at the right frequency and right phase. The color bar represents the displacement in μm. (b) Phase variation of the displacement across the B-mode image. The color bar indicates the phase shift in radians.
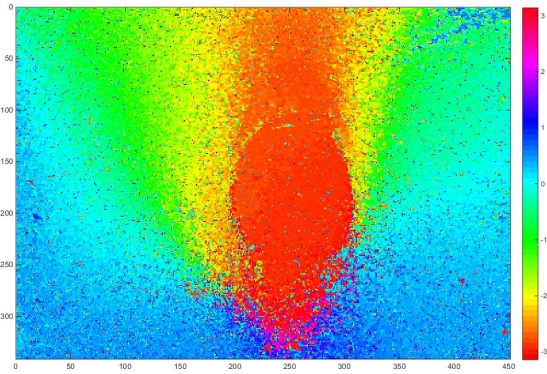
(a)

(b)

Figure 49: Image obtained at solenoid excitation frequency 4 Hz and 20 V_{PP}. The mean displacement within the cylinder is $0.1926 \pm 0.1158\ \mu m$. (a) Magnitude of the displacements occurring at the right frequency and right phase. The color bar represents the displacement in μm. (b) Phase variation of the displacement across the B-mode image. The color bar indicates the phase shift in radians.
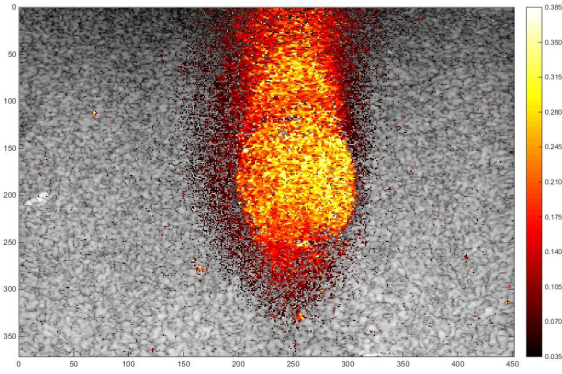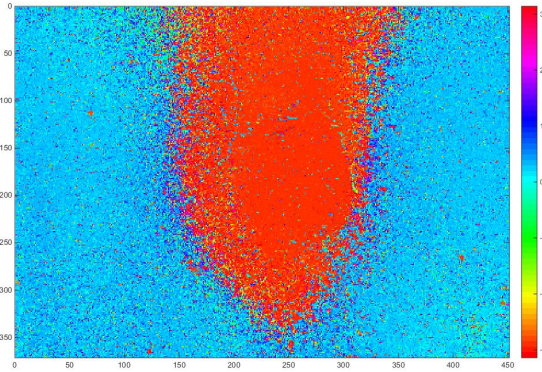
Setup 3

(a)

(b)

Figure 50: Image obtained at solenoid excitation frequency 2 Hz and 30 V_{PP}. The mean displacement within the cylinder is 0.2044 ± 0.1132 μm. (a) Magnitude of the displacements occurring at the right frequency and right phase. The color bar represents the displacement in μm. (b) Phase variation of the displacement across the B-mode image. The color bar indicates the phase shift in radians.
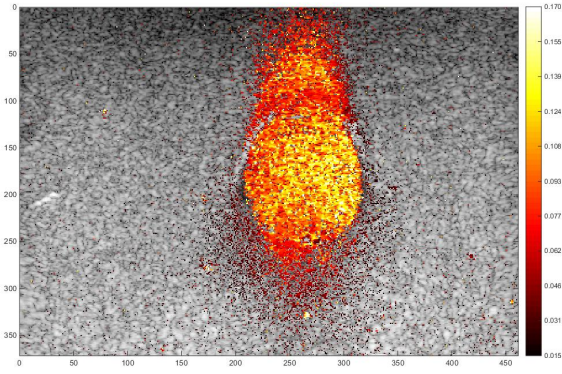
(a)

(b)

Figure 51: Image obtained at solenoid excitation frequency 8 Hz and 30 V_{PP}. The mean displacement within the cylinder is 0.1703 ± 0.1163 μm. (a) Magnitude of the displacements occurring at the right frequency and right phase. The color bar represents the displacement in μm. (b) Phase variation of the displacement across the B-mode image. The color bar indicates the phase shift in radians.
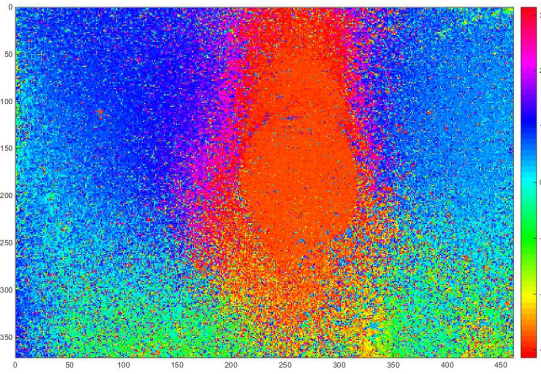
(a)

(b)

Figure 52: Image obtained at solenoid excitation frequency 4 Hz and 10 V_{PP}. The mean displacement within the cylinder is 0.0722 ± 0.0459 μm. (a) Magnitude of the displacements occurring at the right frequency and right phase. The color bar represents the displacement in μm. (b) Phase variation of the displacement across the B-mode image. The color bar indicates the phase shift in radians.
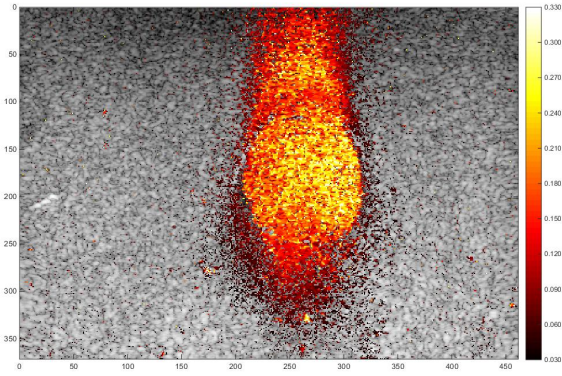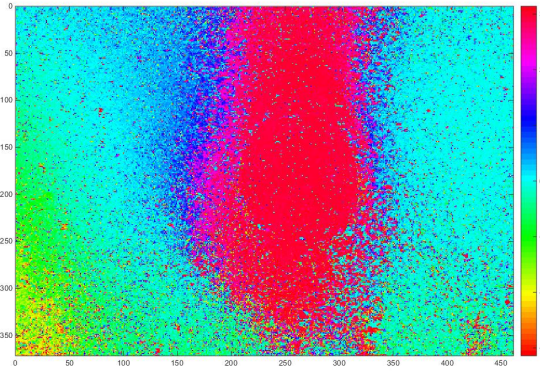
(a)

(b)

Figure 53: Image obtained at solenoid excitation frequency 4 Hz and 20 V_{PP}. The mean displacement within the cylinder is 0.1475 ± 0.0790 μm. (a) Magnitude of the displacements occurring at the right frequency and right phase. The color bar represents the displacement in μm. (b) Phase variation of the displacement across the B-mode image. The color bar indicates the phase shift in radians.
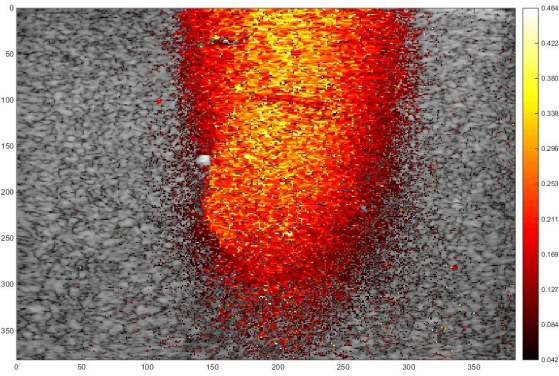
Setup 4

(a)

(b)

Figure 54: Image obtained at solenoid excitation frequency 2 Hz and 30 V_{PP}. The mean displacement within the cylinder is 0.1608 ± 0.0919 μm. (a) Magnitude of the displacements occurring at the right frequency and right phase. The color bar represents the displacement in μm. (b) Phase variation of the displacement across the B-mode image. The color bar indicates the phase shift in radians.
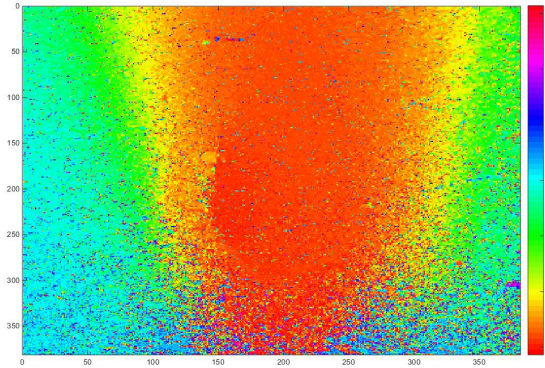
(a)

(b)

Figure 55: Image obtained at solenoid excitation frequency 8 Hz and 30 V_{PP}. The mean displacement within the cylinder is 0.1242 ± 0.0715 μm. (a) Magnitude of the displacements occurring at the right frequency and right phase. The color bar represents the displacement in μm. (b) Phase variation of the displacement across the B-mode image. The color bar indicates the phase shift in radians.
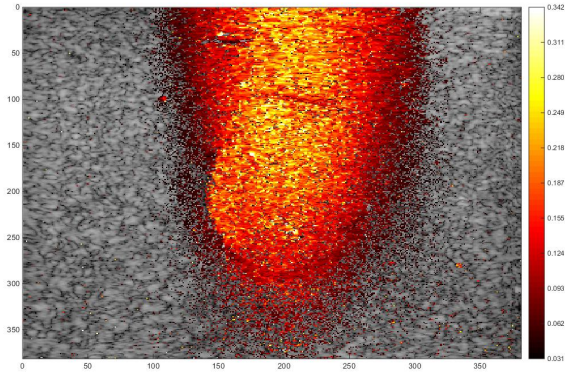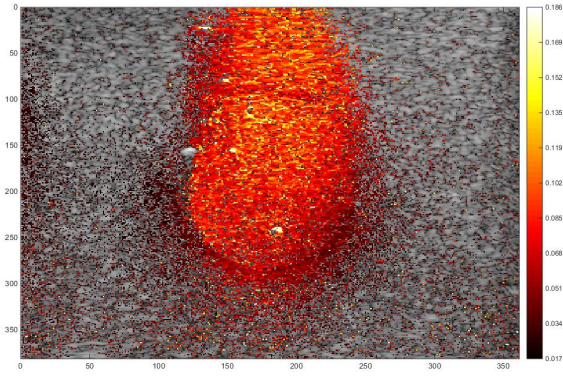
(a)
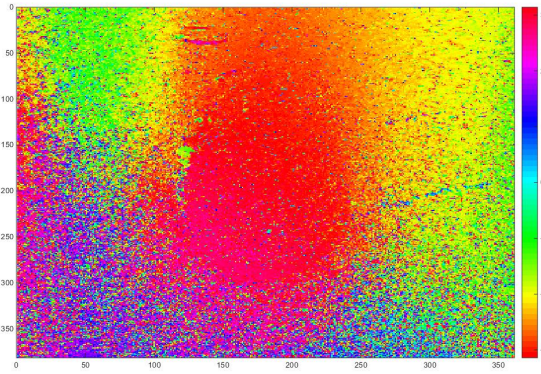
(b)

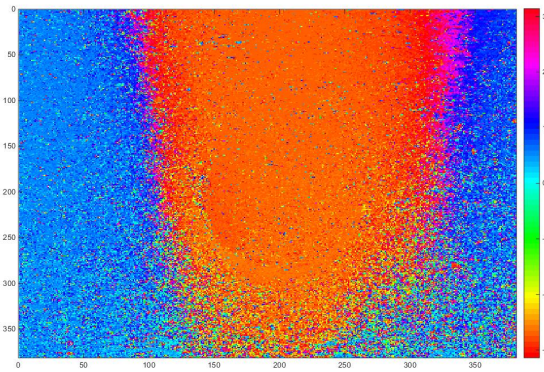Figure 56: Image obtained at solenoid excitation frequency 4 Hz and 10 V_{PP}. The mean displacement within the cylinder is 0.0554 ± 0.0379 μm. (a) Magnitude of the displacements occurring at the right frequency and right phase. The color bar represents the displacement in μm. (b) Phase variation of the displacement across the B-mode image. The color bar indicates the phase shift in radians.

(a)

(b)

Figure 57: Image obtained at solenoid excitation frequency 4 Hz and 20 V_{PP}. The mean displacement within the cylinder is 0.1044 ± 0.0612 μm. (a) Magnitude of the displacements occurring at the right frequency and right phase. The color bar represents the displacement in μm. (b) Phase variation of the displacement across the B-mode image. The color bar indicates the phase shift in radians.
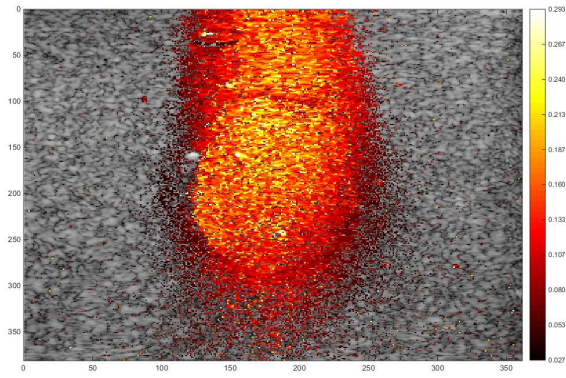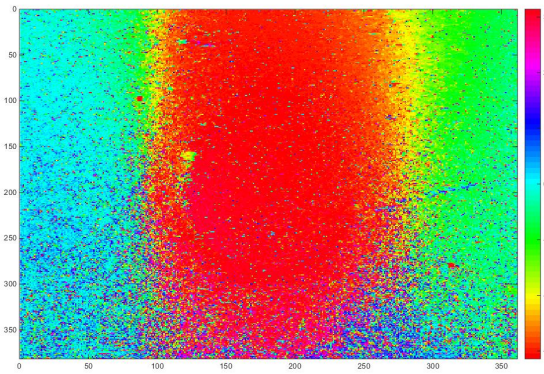
COMSOL

This section contains images from the simulations that was based on values obtained in the elasticity measurements in the practical part of this project, see section 5.1.1 and table 3. The values for Poisson's ratio are based on values found in literature.
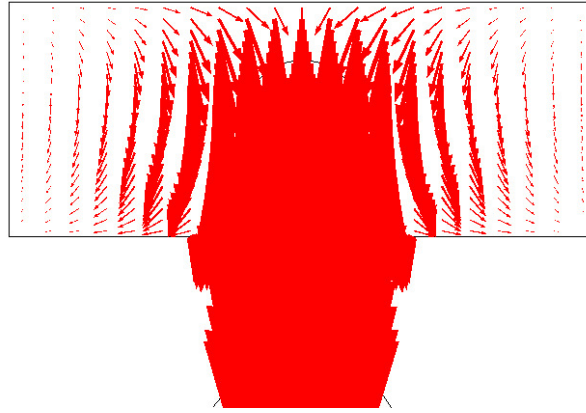
(a)
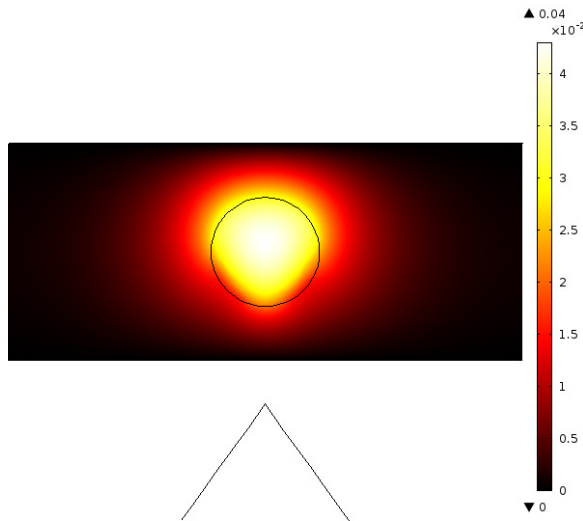
(b)

Figure 58: Correspond to Setup 1, with the elastic properties set to $E = 2800$ Pa and $\nu = 0.42$ for the surrounding and $E = 5300$ Pa and $\nu = 0.42$ for the cylinder. (a) Displacement field in both vertical and horizontal direction. (b) Absolute displacement in the vertical direction.
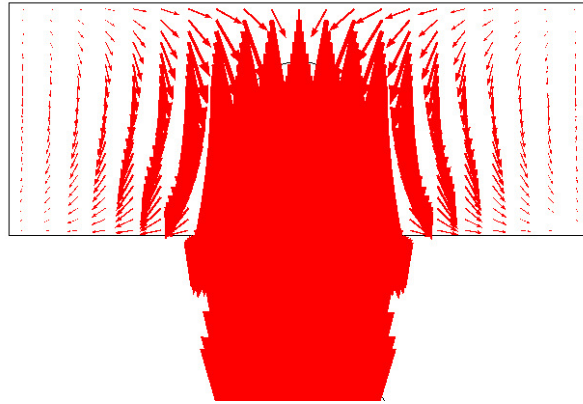
(a)
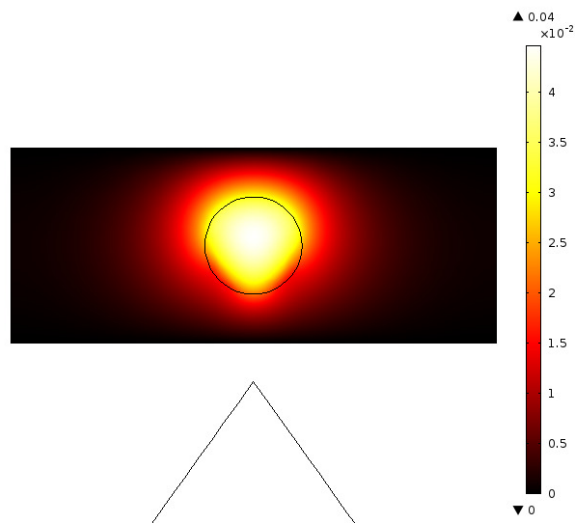
(b)

Figure 59: Correspond to Setup 3, with the elastic properties set to $E = 5300$ Pa and $\nu = 0.42$ for the surrounding and $E = 2800$ Pa and $\nu = 0.42$ for the cylinder. (a) Displacement field in both vertical and horizontal direction. (b) Absolute displacement in the vertical direction.
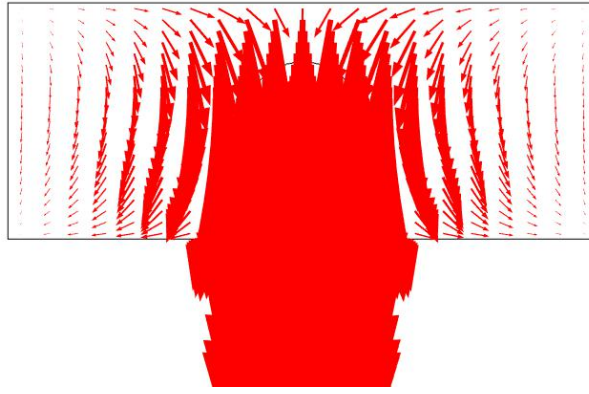
(a)
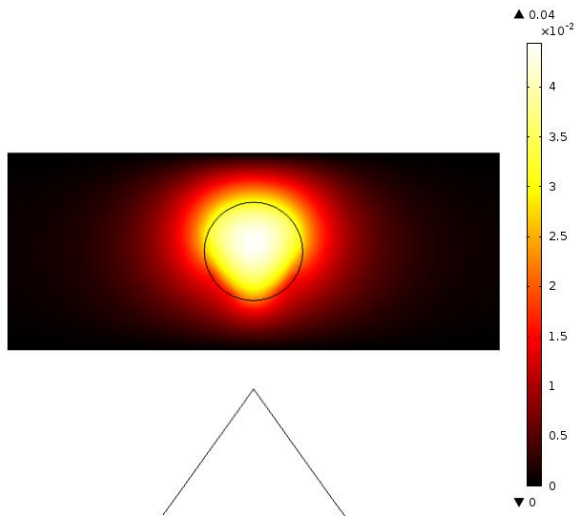
(b)

Figure 60: Correspond to Setup 4, with the elastic properties set to $E = 5800$ Pa and $\nu = 0.42$ for the surrounding and $E = 2800$ Pa and $\nu = 0.42$ for the cylinder. (a) Displacement field in both vertical and horizontal direction. (b) Absolute displacement in the vertical direction.
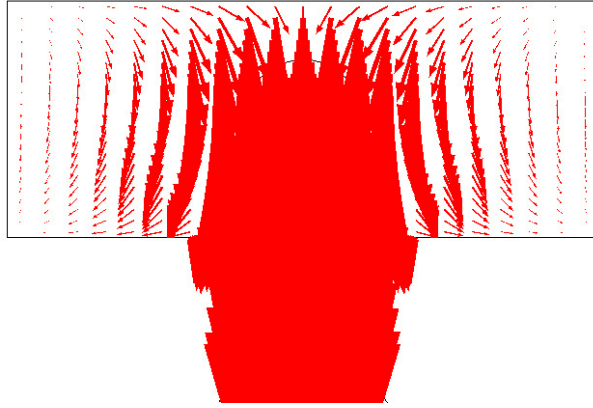
(a)
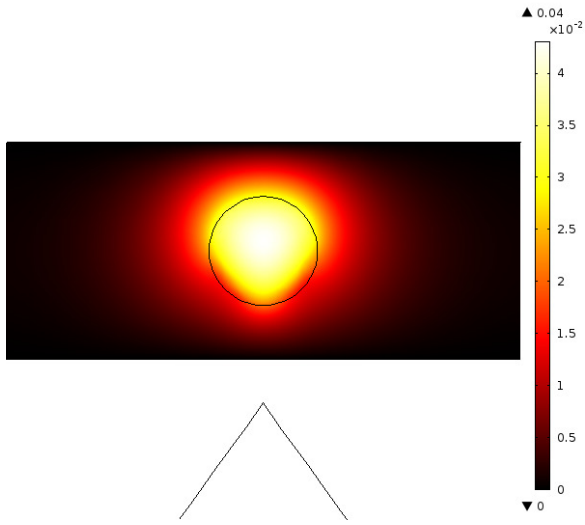
(b)

Figure 61: A phantom with the same elastic properties for both surrounding and cylinder. The Young's modulus is set to $E = 2800$ Pa and Poisson's ratio to $\nu = 0.42$. (a) Displacement field in both vertical and horizontal direction. (b) Absolute displacement in the vertical direction.
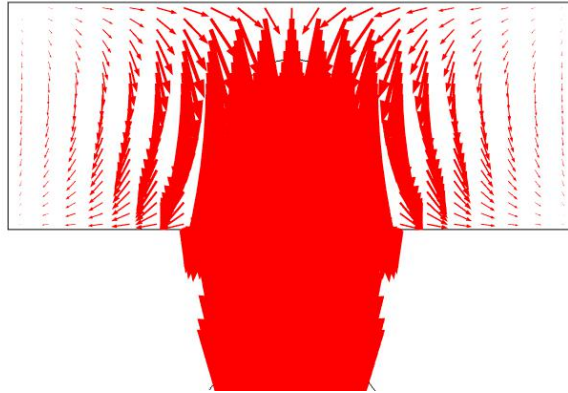
(a)
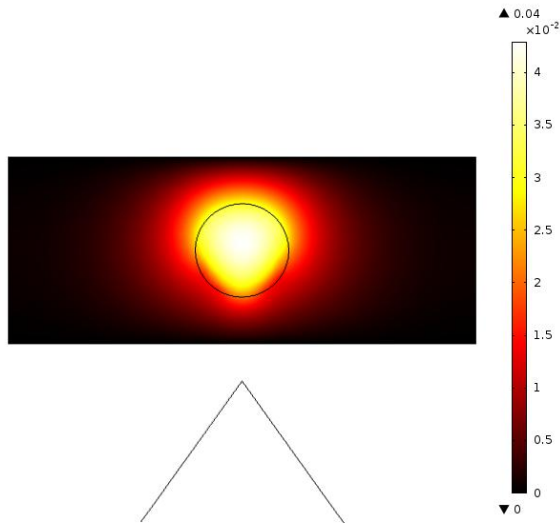
(b)

Figure 62: A phantom with the same elastic properties for both surrounding and cylinder. The Young's modulus is set to $E = 21$ kPa and Poisson's ratio to $\nu = 0.42$. (a) Displacement field in both vertical and horizontal direction. (b) Absolute displacement in the vertical direction.

References

Buscombe, J., G. Paganelli, Z. Burak, W. Waddington, J. Maublant, E. Prats, H. Palmedo, O. Schillaci, L. Maffioli, M. Lassmann, C. Chiesa, E. Bombardieri, and A. Chiti (2007). "Sentinel node in breast cancer procedural guidelines". In: *European Journal of Nuclear Medicine & Molecular Imaging* 34.12, pp. 2154–2159.

ColorFabb (2015a). *Leaf Green*. URL: http://colorfabb.com/leaf-green (visited on 05/04/2015).

— (2015b). *PLA/PHA*. URL: http://colorfabb.com/pla-pha (visited on 05/04/2015).

COMSOL, M. (2015). *The Platform for Physics-Based Modeling and Simulation*. URL: http://www.comsol.se/comsol-multiphysics (visited on 06/09/2015).

Dahllöv, A. (2015a). *Bröstcancer*. URL: http://www.1177.se/Skane/Tema/Cancer/Cancerformer-och-fakta/Cancerformer/Brostcancer/ (visited on 06/02/2015).

— (2015b). *Operation vid bröstcancer*. URL: http://www.1177.se/Skane/Tema/Cancer/Under-och-efter-behandling/Behandlingar/Operation-vid-brostcancer/ (visited on 06/02/2015).

Duboeuf, F., H. Liebgott, A. Basarab, E. Brusseau, P. Delachartre, and D. Vray (2007). "Static mechanical assessment of elastic Young's modulus of tissue mimicking materials used for medical imaging". In: *Annual International Conference of the IEEE Engineering in Medicine and Biology - Proceedings*. 29th Annual International Conference of IEEE-EMBS, Engineering in Medicine and Biology Society, EMBC'07, pp. 3450–3453.

Evertsson, M., M. Cinthio, S. Fredriksson, F. Olsson, H. Persson, and T. Jansson (2013). "Frequency- and phase-sensitive magnetomotive ultrasound imaging of superparamagnetic iron oxide nanoparticles." In: *IEEE Transactions on Ultrasonics Ferroelectrics & Frequency Control* 60.3, p. 481.

Evertsson, M., P. Kjellman, M. Cinthio, S. Fredriksson, R. in 't Zandt, H. Persson, and T. Jansson (2014). "Multimodal detection of iron oxide nanoparticles in rat lymph nodes using magnetomotive ultrasound imaging and magnetic resonance imaging." In: *IEEE Transactions on Ultrasonics Ferroelectrics & Frequency Control* 61.8, p. 1276.

Fredriksson, S. and H. Toftevall (2015). GeccoDots AB.

Fromageau, J., E. Brusseau, D. Vray, G. Gimenez, and P. Delachartre (2003). "Characterization of PVA cryogel for intravascular ultrasound elasticity imaging." In: *IEEE Transactions on Ultrasonics, Ferroelectrics and Frequency Control* 50.10, pp. 1318–1324.

Gherghe, M., C. Bordea, and A. Blidaru (2015). "Clinical Significance of the Lymphoscintigraphy in the Evaluation of Non-axillary Sentinel Lymph Node Localization in Breast Cancer". In: *Chirurgia* 110.1, pp. 26–32.

Griffiths, D. J. (2008). *Introduction to Electrodynamics*. Pearson Education, Inc.

Hoskins, P. R., K. Martin, and A. Thrush (2010). *Diagnostic Ultrasound: Physics and Equipment*. Second. Cambridge University Press.

Jansson, T., M. Evertsson, E. Atile, R. Andersson, S. Fredriksson, H. Persson, I. Svensson, and M. Cinthio (2014). "Induced tissue displacement in magnetomotive ultrasound imaging - simulations and experiments". In: *Ultrasonics Symposium (IUS), 2014 IEEE International*, pp. 639–642.

Junghwan, O., M. Feldman, K. Jeehyun, C. Condit, S. Emelianov, and T. Milner (2006). "Detection of magnetic nanoparticles in tissue using magneto-motive ultrasound". In: *Nanotechnology* 17.16, pp. 4183–4190.

Keshtgar, M. R. S. and P. J. Ell (1999). "Sentinel lymph node detection and imaging". In: *European Journal of Nuclear Medicine* 26.1, pp. 57–67.

Mehrmohammadi, M., T.-H. Shin, M. Qu, P. Kruizinga, R. L. Truby, J.-H. Lee, J. Cheon, and S. Y. Emelianov (2013). "In vivo pulsed magneto-motive ultrasound imaging using high-performance magnetoactive contrast nanoagents". In: *Nanoscale* 5 (22), pp. 11179–11186. DOI: 10.1039/C3NR03669C.

Oldenburg, A., V. Crecea, S. Rinne, and S. Boppart (2008). "Phase-resolved magnetomotive OCT for imaging nanomolar concentrations of magnetic nanoparticles in tissues." In: *Optics Express* 16.15, pp. 11525–11539.

Qu, M. (1.), S. (1.) Mallidi, M. (1.) Mehrmohammadi, R. (1.) Truby, K. (1.) Homan, P. (1.) Joshi, Y.-S. (1.) Chen, 2.) Sokolov K. (1, and S. (1.) Emelianov (2011). "Magneto-photo-acoustic imaging." In: *Biomedical Optics Express* 2.2, pp. 385–396.

Schenck, J. (2005). "Physical interactions of static magnetic fields with living tissues." In: *Progress in Biophysics & Molecular Biology* 87.2, pp. 185–204.

Sigma-Aldrich (2015). *Poly(vinyl alcohol)*. URL: http://www.sigmaaldrich.com/catalog/product/aldrich/341584?lang=en&region=SE&cm_mmc=Google_Material%20Science-_-search-_-Polymer%20Science%20PDP%20Europe_Hydrophilic%20Polymers%20-%20Europe-_-POLY%20VINYL%20ALCOHOL_Phrase&cm_guid=1-_-10000000000000166288-_-33887343862&gclid=CLLdkqjp1MQCFabHtAodE1UA0g (visited on 05/04/2015).

Sneddon, I. N. (1965). "The Relaxation Between Load and Penetration In the Axisymmetric Boussinesq Problem for a Punch of Arbitrary Profile". In: *Int. J. Engng Sci.* 3, pp. 47–57.

Somasundaram, K. S., D. W. Chicken, and M. R. S. Keshtgar (2007). "Detection of the sentinel lymph node in breast cancer." In: *British Medical Bulletin* 84.1, pp. 117–131.

Ultimaker (2015). *Ultimaker 2*. URL: https://ultimaker.com/en/products/ultimaker-2-family/ultimaker-2 (visited on 05/04/2015).

VisualSonics (2015). *Vevo® 2100 System*. URL: http://www.visualsonics.com/products/vevo-2100 (visited on 06/10/2015).